Iron (II/III) Halide Complexes Promote the Interconversion of Nitric Oxide and *S*-nitrosothiols through Reversible Fe-S Interaction

Anna L. Poptic,[†] and Shiyu Zhang*,[†]

[†]Department of Chemistry & Biochemistry, The Ohio State University, 100 West 18th Avenue, Columbus, Ohio 43210, United States

ABSTRACT: Heme and non-heme iron in biology mediate the storage/release of NO• from *S*-nitrosothiols as a means to control the biological concentration of NO•. Despite their importance in many physiological processes, the mechanisms of N-S bond formation/cleavage at Fe centers have been controversial. Herein, we report the interconversion of NO• and *S*-nitrosothiols mediated by Fe^{II}/Fe^{III} chloride complexes. The reaction of two equivalents of *S*-nitrosothiol (Ph_3CSNO) with $[Cl_6Fe^{II}_2]^{2-}$ results in facile release of NO• and formation of iron(III) halothiolate. Detailed spectroscopic studies, including in situ UV-vis, IR, and Mössbauer spectroscopy, support the interaction of the S−atom with the Fe^{II} center. This is in contrast to the proposed mechanism of NO• release from the well-studied "red product" κ^1-N bound *S*-nitrosothiol Fe^{II} complex, $[(CN)_5Fe(\kappa^1\text{-N-RSNO})]^{3-}$. Additionally, Fe^{III} chloride can mediate NO• storage through the formation of *S*-nitrosothiols. Treatment of iron(III) halothiolate with two equivalents of NO• regenerates Ph_3CSNO with the Fe^{II} source trapped as the $S = 3/2$ {FeNO}[7] species $[Cl_3FeNO]^-$, which is inert towards further coordination and activation of *S*-nitrosothiols. Our work demonstrates how labile iron can mediate the interconversion of NO•/thiolate and *S*-nitrosothiol, which has important implications for how Nature manages the biological concentration of free NO•.

INTRODUCTION

Nitric oxide (NO•) is a crucial secondary signaling molecule responsible for the regulation of a range of biological processes, including immune response, smooth muscle relaxation, and neurotransmission.[1] However, NO• has a short lifetime *in vivo* and quickly reacts with the bio-available oxygen and superoxide, forming reactive oxygen and reactive nitrogen species.[2] To mitigate the formation of these reactive species, Nature has developed specific regulatory strategies that store NO• as air-stable *S*-nitrosothiols (RSNOs).[3] RSNOs can also serve as signaling molecules to participate in the *S*-nitrosation of proteins, which is a precisely regulated post-translational modification. Dysregulation of RSNO homeostasis has been linked to several diseases, such as Alzheimer's disease and Parkinson's disease, cancer, diabetes, etc..[4,5]

Formation of *S*-nitrosothiols from free NO• and thiol requires one-electron oxidation, which can be facilitated by the single-electron accepting abilities of Fe^{III} or Cu^{II}. Conversely, Fe^{II} and Cu^I can act as one-electron reducing agents to promote the release of NO• from *S*-nitrosothiols via cleavage of the S-N bond.[3,6–9] Several biological iron centers have been implicated in RSNO decomposition/formation. For example, heme-iron proteins, such as cytochrome *c*, are responsible for the coupling of NO• and low-mass thiols to RSNOs, i.e., *S*-nitrosoglutathione (GSNO) or *S*-nitroso-*L*-cysteine (CysSNO).[4] In addition to enzymatic heme-iron centers, exposure of NO• to intracellular labile iron has been associated with increased levels of protein *S*-nitrosation with simultaneous formation of dinitrosyl iron complexes (DNICs).[10,11] Moreover, the release of NO• from the blood pressure medication sodium nitroprusside (SNP) $[Na]_2[Fe(CN)_5(NO)]$ is thought to proceed through the decomposition of an iron(II) *S*-nitrosothiol adduct, $[Fe(CN)_5(\kappa^1\text{-N-RSNO})]^{3-}$, known as the "red product".[12,13]

Despite the importance of iron centers in facilitating the formation/decomposition of *S*-nitrosothiols, the discrete molecular mechanisms of N-S bond formation/cleavage at iron sites remain controversial. For example, two mechanisms have been proposed for *S*-nitrosothiol formation at heme-iron sites. The first involves nucleophilic attack of an iron nitrosyl {FeNO}[6] species by a thiolate (Scheme 1, top), whereas the second invokes an Fe^{III}–thiolate intermediate undergoing further reaction with free NO• (Scheme 1, bottom).[14,15] Despite the structural characterization of *S*-nitrosated heme-iron proteins,[16] spectroscopic support for both mechanisms exists.[16–18]

Scheme 1
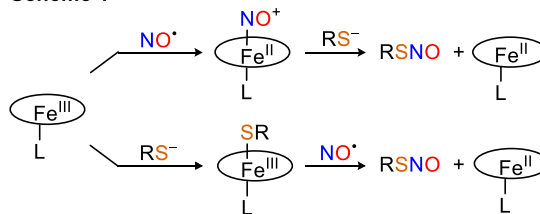
Significant research efforts have also been devoted to understanding the binding mode of *S*-nitrosothiols to Fe centers (κ^1-N vs. κ^1-S) during NO• release from SNP (Scheme 2). Spectroscopic studies suggest that the "red-product" $[Fe(CN)_5(\kappa^1\text{-N-RSNO})]^{3-}$ extrudes a thiyl (RS•) radical to form a $[(CN)_5FeNO]^{3-}$ complex ({FeNO}[7]) which then releases free NO•.[19,20] However, both experimental[8,21,22] and computational[23,24] studies have demonstrated the thiyl radical (RS•) expulsion process in Scheme 2 should be unfavorable since κ^1-N coordination of *S*-nitrosothiols strengthens the S-N bond (Scheme 3). Furthermore, the currently proposed mechanism does not explain the rapid vasodilatory effect of SNP, given the slow rate of NO• liberation from the {FeNO}[7] $[(CN)_5FeNO]^{3-}$ ($k = 5.0 \times 10^{-5}$ s^{-1}, Scheme 2).[25]

Scheme 2
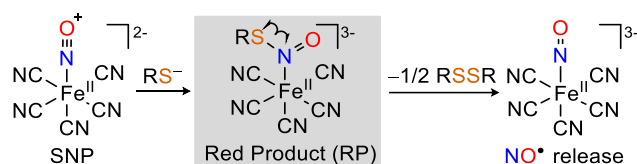
*Too slow to explain the fast vasodilatory effect of SNP*

As the debate for the mechanisms of *S*-nitrosothiol formation and decomposition at iron sites continue, the mechanism of RSNO formation mediated by the labile iron pool (LIP) also remains ambiguous. Iron within the LIP is present in both Fe^{II}/Fe^{III} oxidation states and can be coordinated by various weak field ligands to form high-spin Fe^{II}/Fe^{III} complexes.[10,26–29] While Kim and Lippard have investigated the reactivity of NO• with synthetic iron-sulfur clusters[30–33] and iron(II) thiolates,[34–37] other simple Fe^{II}/Fe^{III} coordination complexes relevant to the LIP and NO•/*S*-nitrosothiol interconversion still warrant continued investigation.

Scheme 3
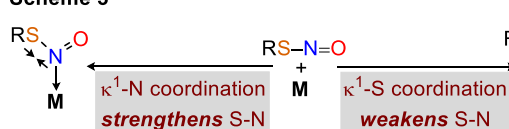
Herein, we employ Fe^{II}/Fe^{III} chloride complexes as simplified models for LIP to investigate the potential roles of Fe^{II}/Fe^{III} in RSNO formation/decomposition. We demonstrate that reaction of RSNO with Fe^{II} chloride complexes leads to the facile release of NO• from RSNO (Scheme 4). Spectroscopic studies suggest that the Fe^{II} center interacts with the S-atom before its conversion to iron(III)–halothiolate and NO•. The NO• release from RSNO is reversible, and in the presence of an additional equivalent of NO•, the iron(III)–halothiolate captures NO• to afford RSNO. The Fe^{II} chloride by-product is trapped by a second equivalent of NO• to form stable {FeNO}[7] complexes that are inert toward catalytic decomposition of RSNO. This unique property of high-spin iron complexes may be a strategy Nature employs to reversibly regulate the bio-availability of free nitric oxide.

Scheme 4
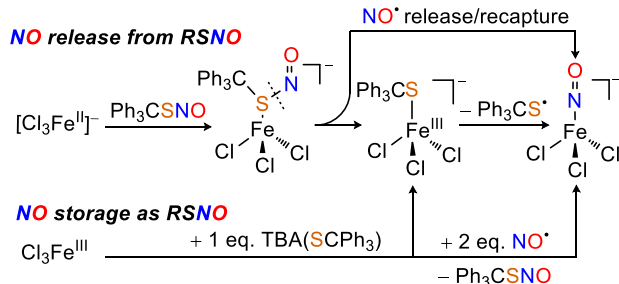
RESULTS AND DISCUSSION

Reactivity of Fe^{II} chloride with *S*-nitrosothiols. We began our investigation by preparing an iron(II) halide complex soluble in aprotic solvents. Treatment of PPNCl (PPN = bis(triphenylphosphine)iminium) with $Fe^{II}Cl_2$ in acetone affords PPN$_2$[$Fe^{II}_2Cl_6$]. The spectroscopic characterizations of the PPN$_2$[$Fe^{II}_2Cl_6$] complex match those reported in the literature.[38] The analogous TBA salt of iron(II) trichloride was isolated as colorless crystals by the addition of TBACl (TBA =

tetrabutylammonium) to $Fe^{II}Cl_2$. Single-crystal X-ray diffraction analysis indicates that the Fe^{II} centers exist in two types of coordination environments, as [$Fe^{II}_2Cl_6$]$^{2-}$ and monomeric [$Cl_3Fe^{II}(H_2O)$]$^-$ (Figure S26). Next, we monitored the reaction of [$Fe^{II}_2Cl_6$]$^{2-}$ with Ph$_3$CSNO with UV-vis spectroscopy at low temperature. The structural difference between the PPN and TBA salts of the Fe^{II} chlorides in the solid-state does not impact their reactivity with *S*-nitrosothiols (Figures S7, S8). Addition of two equivalents of Ph$_3$CSNO to [$Fe^{II}_2Cl_6$]$^{2-}$ in a 1:1 mixture of THF and MeCN at −50 °C affords a dark brown complex with UV-vis absorption bands at 520 nm (ε = 1000 M^{-1} cm^{-1}) and 630 nm (ε = 970 M^{-1} cm^{-1}) (Figure 1, brown trace), which slowly converts to a green species at room temperature with absorbances at 365 nm (ε = 1080 M^{-1} cm^{-1}), 480 nm (ε = 410 M^{-1} cm^{-1}), and 660 nm (ε = 320 M^{-1} cm^{-1}) (Figure 1, green trace). The final green complex was identified as S = 3/2 TBA[Cl$_3$FeNO], which can be independently synthesized by treatment of [$Fe^{II}_2Cl_6$]$^{2-}$ with NO• (Figure S4).[39] Based on the absorptivity of [Cl$_3$FeNO]$^-$, the yield of TBA[Cl$_3$FeNO] was approximately quantitative. The [Cl$_3$FeNO]$^-$ anion was observed first by Kohlschütter,[40] and structurally characterized by Van Eldik,[41] Beck,[42] and Klüfers.[39] The S = 3/2 spin state of [Cl$_3$FeNO]$^-$ was established recently based on SQUID measurement[39] and our Evans method study (see supporting information). The [Cl$_3$FeNO]$^-$ complex is remarkably stable to oxygen and moisture, and no decomposition of PPN[Cl$_3$FeNO] solid was observed even after storage under ambient conditions for several days.
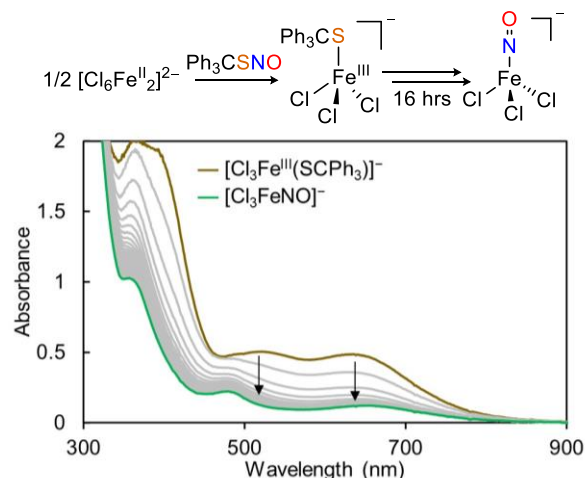

Figure 1. In situ UV-vis spectra of the treatment of [Fe_2Cl_6]$^{2-}$ with two equivalents of Ph$_3$CSNO at −50 °C in 1:1 THF/CH$_3$CN (0.5 mM). The brown intermediate [Cl$_3$Fe(SCPh$_3$)]$^-$ was eventually converted to [Cl$_3$FeNO]$^-$ (green trace).

Two possible mechanisms could explain the formation of [Cl$_3$FeNO]$^-$ (Scheme 5). Based on the proposed mechanism of NO• release from SNP (Scheme 2), one could envision coordination of Ph$_3$CSNO to the Fe^{II} center to form a Fe^{II} κ^1-N *S*-nitrosothiol adduct, followed by thiyl radical extrusion to afford [Cl$_3$FeNO]$^-$ (Mechanism A, Scheme 5 top). However, Mechanism A contradicts the chemical reactivity of metal *S*-nitrosothiols described in Scheme 3.[8,21,22] Therefore, an alternative mechanism in which the Fe^{II} center interacts with the S-atom warrants consideration (Mechanism B, Scheme 5 bottom). In this case, NO• is released from [Cl$_3$Fe(κ^1-S-Ph$_3$CSNO)]$^-$ then recaptured by [$Fe^{II}_2Cl_6$]$^{2-}$ generated from the decomposition of

2

$[Cl_3Fe^{III}$-$SCPh_3]^-$. The key difference between these two mechanisms is the identity of the brown intermediate prior to the formation of $[Cl_3FeNO]^-$ (highlighted in gray, Scheme 5). In Mechanism A, the brown intermediate should be $[Cl_3Fe(\kappa^1$-N-$Ph_3CSNO)]^-$, while for Mechanism B it should be either $[Cl_3Fe(\kappa^1$-S-$Ph_3CSNO)]^-$ or $[Cl_3Fe^{III}$-$SCPh_3]^-$.

Scheme 5
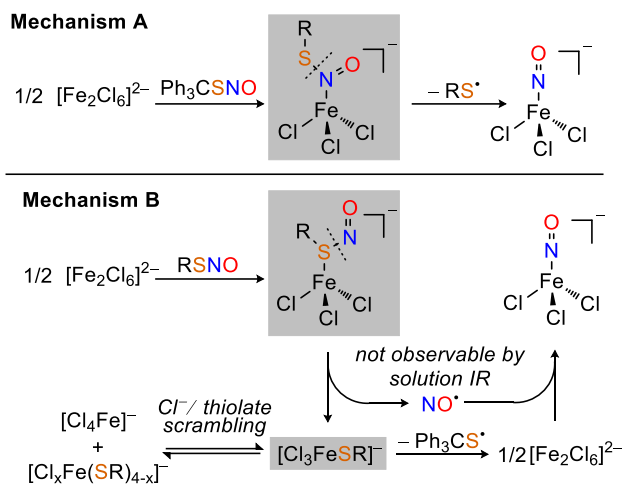
Characterization of the Fe^{III} halothiolate intermediate. To further discern the two proposed mechanisms, we set out to identify the initial brown intermediate that absorbs at 520 nm and 630 nm. Anticipating it might be the iron(III)–halothiolate $[Cl_3Fe^{III}$-$SCPh_3]^-$, we attempted to generate it from an independent reaction between $TBA[Cl_4Fe^{III}]$ and $NaSCPh_3$. As shown in Figure 2, the in situ UV-vis spectrum of the reaction of $TBA[Cl_4Fe^{III}]$ with one equivalent of $NaSCPh_3$ in MeCN/THF (red trace) shows a good match with the brown intermediate. Further, the reaction between $FeCl_3$ and $TBA(SCPh_3)$ leads to the formation of the same spectrum, albeit at a lower spectroscopic yield (Figure S10). In addition, the predicted UV-vis spectrum of $[Cl_3Fe^{III}$-$SCPh_3]^-$ by time-dependent density functional theory (TD-DFT) at the TPSSh/def2-TZVP level correlates well with the experimental data (Figure S26). Unfortunately, we were unable to structurally characterize the putative $[Cl_3Fe^{III}$-$SCPh_3]^-$ due to
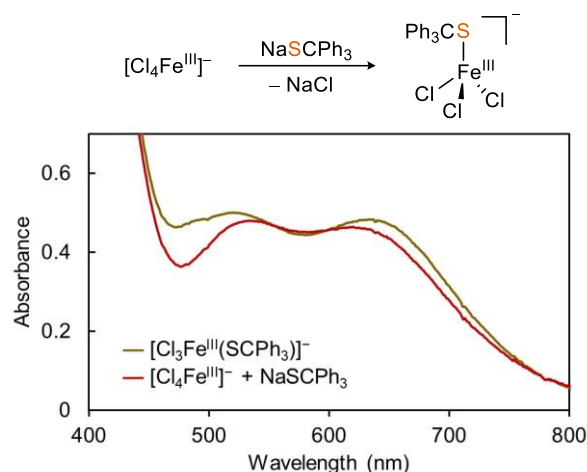
Figure 2. Comparison of initial UV-vis spectra resulting from the reaction between $[Fe_2Cl_6]^{2-}$ and Ph_3CSNO at −50 °C in 1:1 THF/CH₃CN (0.5 mM, brown trace); the reaction between $TBA[Cl_4Fe^{III}]$ and one equivalent of $NaSCPh_3$ at −20 °C (0.5 mM, red trace).

complicated ligand scrambling that generates other $[Cl_xFe^{III}$-$(SCPh_3)_{4-x}]^-$ (x = 1, 2, 3, 4) as well as decomposition of $[Cl_3Fe^{III}$-$SCPh_3]^-$ to Ph_3CS-$SCPh_3$ and $[Fe^{II}_2Cl_6]^{2-}$ (see supporting information). Titration experiments of $NaSCPh_3$ into $TBA[Cl_4Fe^{III}]$, and $TBA(SCPh_3)$ into $FeCl_3$ at −40 °C show formation of multiple species from a 1:1 to 4:1 thiolate to Fe^{III} ratio (Figures S11, S12). Regardless of molecular connectivity, the ratio of Cl^-: Fe^{III}: Ph_3CS^- remains as 3:1:1 under the experimental conditions employed; therefore, we will refer to the collective products of Cl_3Fe^{III} and Ph_3CS^- as $[Cl_3Fe^{III}$-$SCPh_3]^-$ for simplicity.

Analysis of the brown intermediate with Mössbauer spectroscopy further supports its assignment as an Fe^{III} thiolate species. Independent generation of $[Cl_3^{57}Fe^{III}(SCPh_3)]^-$ from the reaction between $TBA[Cl_4^{57}Fe^{III}]$ and one equivalent of $NaSCPh_3$ displays a Mössbauer spectrum similar to that produced from the reaction between $TBA_2[Cl_6^{57}Fe^{II}_2]$ and two equivalents of Ph_3CSNO (See supporting information, Figures S18, S19). Both spectra display peaks corresponding to two major species—the first one (ca. 40%) exhibiting isomer shift and quadrupole splitting values identical to that of $TBA_2[Cl_6^{57}Fe^{II}_2]$ ($\delta = 1.16$ mm s⁻¹, $|\Delta E_Q| = 2.86$ mm s⁻¹ (Figure S14)). The second component (ca. 60%) displays an isomer shift of $\delta = 0.38$ mm s⁻¹ and quadrupole splitting value of $|\Delta E_Q| = 0.94$ mm s⁻¹, which was assigned as $[Cl_3^{57}Fe^{III}(SCPh_3)]^-$. These parameters are different from those of $TBA[Cl_4^{57}Fe^{III}]$ (Figure S17), which has an isomer shift value of $\delta = 0.23$ mm s⁻¹ and a quadrupole splitting of $|\Delta E_Q| = 0.53$ mm s⁻¹ (Table 1).

Table 1. Solution Mössbauer parameters

Complex (major component)	δ (mm/s)	ΔE_Q (mm/s)
$TBA_2[Cl_6^{57}Fe^{II}_2]$	1.16	2.86
$TBA[Cl_4^{57}Fe^{III}]$	0.23	0.53
$TBA[Cl_4^{57}Fe^{III}] + NaSCPh_3$	0.38	0.94
$TBA_2[Cl_6^{57}Fe^{II}_2] + 2\,Ph_3CSNO$	0.38	0.93

In situ IR study of the conversion of $[Fe^{II}_2Cl_6]^{2-}$ to $[Cl_3FeNO]^-$ by Ph_3CSNO. The in situ UV-vis and Mössbauer data so far suggest that reaction of $[Fe^{II}_2Cl_6]^{2-}$ with Ph_3CSNO first leads to the formation of an iron(III) halothiolate and free $NO^\bullet$. The iron(III) halothiolate then slowly decomposes to disulfide and $[Fe^{II}_2Cl_6]^{2-}$, which captures free $NO^\bullet$ to form the $[Cl_3FeNO]^-$ complex (Scheme 5, Mechanism B). Further support of Mechanism B was provided by an in situ time-resolved solution IR study. Addition of $[Fe^{II}_2Cl_6]^{2-}$ to a solution with two equivalents of Ph_3CSNO in THF-d_8 at −70 °C results in a decrease of the peak at 1493 cm⁻¹ corresponding to Ph_3CSNO. Upon further warming of the reaction mixture to −50 °C, a new band at 1792 cm⁻¹ appeared, which was attributed to $TBA[Cl_3FeNO]$ (Figure 3A).[39] An ¹⁵N-labeling experiment confirmed that Ph_3CSNO and $[Cl_3FeNO]^-$ were the only species observed with ¹⁵N-sensitive stretches over the course of the reaction (See SI, Figure S21, S22). Importantly, the initial decay of Ph_3CSNO was not accompanied by the formation of $[Cl_3FeNO]^-$ (Figure 3B). The time gap (ca. 90 seconds) between these two events provides further assent that free $NO^\bullet$ was first released into the headspace, where it was unobservable by solution IR until it was recaptured by $[Fe^{II}_2Cl_6]^{2-}$ as $[Cl_3FeNO]^-$, consistent with Mechanism B (Scheme 5, bottom).

3
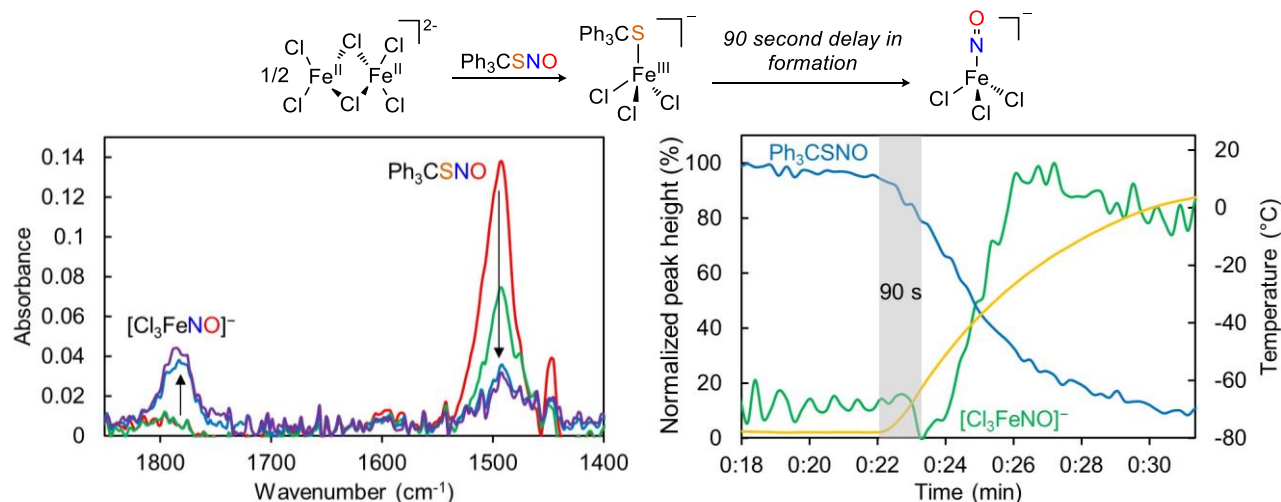
Figure 3. Left: A) In situ solution IR spectra of the reaction between $[Fe_2Cl_6]^{2-}$ and Ph_3CSNO in THF-d_8, 30 mM (from red to purple traces), showing a decrease in $\nu(NO) = 1493$ cm^{-1} (Ph_3CSNO) and the appearance of $\nu(NO) = 1792$ cm^{-1} ($[Cl_3FeNO]^-$) upon warming. B) Normalized peak heights of Ph_3CSNO (blue) and $TBA[Cl_3FeNO]$ (green) versus time and temperature (yellow) shows a 90 second delay (shaded grey) in $TBA[Cl_3FeNO]$ formation.

In situ UV-vis, Mössbauer, and IR spectroscopic studies allow us to conclude that NO$^{\bullet}$ release likely proceeds through coordination of the S-atom to Fe^{II} prior to S-N bond cleavage. Otherwise, the concurrent formation of $[Cl_3FeNO]^-$ and consumption of Ph_3CSNO would be expected. The proposed mechanism is also consistent with the reactivity profile of metal S-nitrosothiol complexes−κ^1-S coordination weakens the S-N bond, making the release of NO$^{\bullet}$ more favorable (Scheme 3).[13]

RSNO formation from putative iron(III) halothiolate As many NO$^{\bullet}$ release/storage mechanisms are reversible in Nature,[8] we next investigated whether the Fe^{II}/Fe^{III} chloride couple can carry out the formation of S-nitrosothiol. Lancaster et al. proposed that the LIP can promote RS-NO bond formation based on the observation that the cellular protein S-nitrosation levels strongly depend on the concentration of labile/chelatable iron.[10,11] To this end, we first generated the putative $[Cl_3Fe^{III}SCPh_3]^-$ by treating Fe$^{III}Cl_3$ with $TBA(SCPh_3)$ at −78 °C and subjected this reaction mixture to sequential additions of NO$^{\bullet}$. In situ solution IR spectroscopy was utilized to monitor and quantify product formation. After the addition of two equivalents of NO$^{\bullet}$ at −78 °C and upon warming the reaction

mixture to −50 °C, we observed concurrent formation of peaks at 1792 cm^{-1} and 1493 cm^{-1} (Figure. 2C), assigned as $[Cl_3FeNO]^-$ and Ph_3CSNO, respectively.[39,45] The estimated yields of $[Cl_3FeNO]^-$ and Ph_3CSNO were 67% and 50%, respectively, based on the IR absorbances (see supporting information, Figures S24, S25). The Fe^{III} center facilitates the oxidative coupling of thiolate and NO$^{\bullet}$ to form Ph_3CSNO by acting as an electron acceptor and undergoing reduction to Fe^{II}, which may be trapped by additional NO$^{\bullet}$ to form $[Cl_3FeNO]^-$. The presence of an additional equivalent of NO$^{\bullet}$ is critical to prevent the reverse reaction, that is, the release of NO$^{\bullet}$ from Ph_3CSNO, as Fe^{II} complexes are known to lead to the decomposition of RSNO to disulfide and NO$^{\bullet}$ (Scheme 6). The robust Fe-NO$^{\bullet}$ interaction impedes the displacement of the NO$^{\bullet}$ ligand by S-nitrosothiol and prevents the catalytic decomposition of RSNO (Scheme 6). Such a "switch effect" of NO$^{\bullet}$ represents a key difference between Fe and Cu mediated S-nitrosothiol formation; the strong interaction between high-spin Fe^{III} (S = 5/2) with NO$^-$ (S = 1) is not shared by Cu.[6] In fact, some of us, and Hayton et al. have shown that the interaction of Cu^{II} and NO$^{\bullet}$ is highly reversible.[46,47]
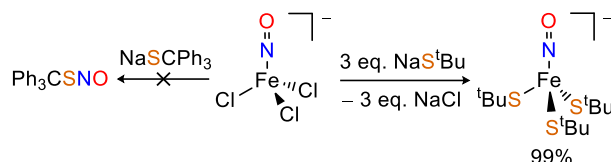
Scheme 6
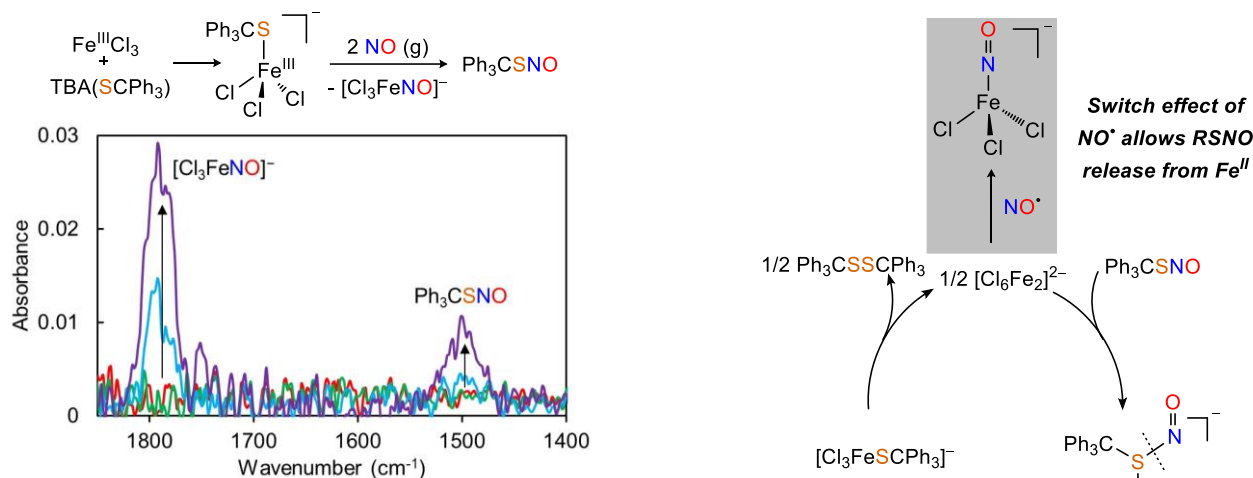
Figure 4. In situ IR spectrum of the reaction between $[Cl_3Fe^{III}SCPh_3]^-$ and 2 eq NO$^{\bullet}$ in 9:1 THF-d_8/CD$_3$CN at −80 °C (30 mM). At −50 °C formation of Ph_3CSNO ($\nu(NO) = 1493$ cm^{-1}) and $TBA[Cl_3FeNO]$ ($\nu(NO) = 1792$ cm^{-1}) was observed.

4

To confirm that [Cl₃FeNO]⁻ does not participate in RS-NO bond formation, we investigated its reaction with thiolate. Treatment of PPN[Cl₃FeNO] with sodium *tert*-butyl thiolate affords a red-colored solution with strong absorbances at 360 nm ($\varepsilon = 6670$ M⁻¹cm⁻¹) and 475 nm ($\varepsilon = 4360$ M⁻¹cm⁻¹) , which were assigned as PPN[(ᵗBuS)₃FeNO].[36] Titration of *tert*-butyl thiolate to a solution of PPN[Cl₃FeNO] in UV-vis spectrometer confirmed the 3:1 stoichiometry (Figure S6). Employing *tert*-butyl thiolate allowed us to calculate the yield of the product [(ᵗBuS)₃FeNO]⁻ based on reported molar extinction coefficients. The spectroscopic yield of [(ᵗBuS)₃FeNO]⁻ was determined to be 99%, indicating that the {FeNO}⁷ motif is robust, while Cl⁻ ligand exchange occurs with ᵗBuS⁻.[36]

Scheme 7

Electronic structure of [Cl₃FeNO]⁻, [Cl₃CuNO]⁻, and Cl₃FeNO The inertness of [Cl₃FeNO]⁻ towards nitrosation of thiolate and the irreversible binding of NO• at [Cl₃Feᴵᴵ]⁻ is a crucial part of Mechanism B proposed in Scheme 5. These properties of [Cl₃FeNO]⁻ are in sharp contrast to its Cu analog [Cl₃CuNO]⁻, which exhibits both reversible binding with NO• and nitrosative reactivity toward thiolates. To gain more insight into the different reactivities of [Cl₃FeNO]⁻ and [Cl₃CuNO]⁻, we utilized complete active space self-consistent field (CASSCF) computations to further understand their electronic structure. Some of us[46] and others[39,46,48,49] have shown that CASSCF calculations can provide a detailed understanding of the correlation of electronic structure and reactivity of metal-nitrosyls. The state-specific CASSCF calculations were performed in each complex's well-established spin state, $S = 3/2$ for [Cl₃FeNO]⁻ and $S = 0$ for [Cl₃CuNO]⁻.[39,46,50] After screening various combinations of metal 3d, NO-σ*, and NO-π* orbitals, we chose an active-space of [9e,13o] for [Cl₃FeNO]⁻ and [10e,13o] for [Cl₃CuNO]⁻. These active spaces include (i) bonding and antibonding orbitals of NO-π* with metal-$d_{xz/yz}$, (ii) bonding and antibonding orbitals of NO-σ* with metal-d_{z2},

(iii) nonbonding $d_{x2-y2/xy}$ as well as (iv) the next five unoccupied orbitals lowest in energy, which are often based on metal 4d or ancillary ligands Cl⁻ (See supporting information)). We found that 4d orbitals and ancillary orbitals have little effect on the results of the calculations, consistent with previous studies by Klüfers.[39,49] To computationally estimate the amount of NO⁻/•/⁺ character in each complex, a valence bond-like interpretation of the CAS wavefunction was applied by following the method laid out by Radón et al.[51] The amount of NO⁻/•/⁺ character in each species is summarized in Table 2. Intuitively, higher percentages of Mⁿ⁺¹-NO⁺ character correlates to NO⁺ transfer (nitrosative) ability, while Mⁿ-NO• corresponds to free NO• release. We found the CASSCF results to be roughly consistent with the observed reactivity of [Cl₃FeNO]⁻ and [Cl₃CuNO]⁻. Specifically, [Cl₃FeNO]⁻ exhibits the lowest NO• character (38%) and NO⁺ character (2%), consistent with its inability to release free NO• and perform *S*-nitrosation. [Cl₃CuNO]⁻ exhibits significant NO• and NO⁺ character (86% and 10%, respectively) and is capable of both NO• release and *S*-nitrosation.[46]

Table 2. Results of valence-bond analysis of metal nitrosyls

Res. Structure	[Cl₃FeNO]⁻	[Cl₃CuNO]⁻	Cl₃FeNO
M−NO⁻	52%	1%	0.25 %
M−NO•	40%	86%	93%
M−NO⁺	2%	10%	4%
others	5%	3%	2%

We were curious as to whether this qualitative analysis would allow us to predict the NO⁺ reactivity of Cl₃FeNO, the product of the one-electron oxidation of [Cl₃FeNO]⁻. This theoretical interaction of FeᴵᴵᴵCl₃ with NO• would result in an {FeNO}⁶ complex with a spin ($S = 2$), which would be more likely to exhibit NO⁺ transferring ability. The geometry of putitive Cl₃FeNO complex was optimized with DFT in a variety of spin states ($S = 0, 1, 2$). The two known non-heme {FeNO}⁶ complexes both have an experimentally and computationally determined $S = 1$ (Feᴵⱽ-NO⁻) ground state;[52] however, optimization by B3LYP/def2-TZVP determined the $S = 2$ state in Cl₃FeNO to be the lowest in energy by −20.3 kcal/mol. CASSCF calculation on the $S = 2$ spin state showed highly covalent bonding character between the Fe d_{z2} and NO p_x orbitals with 1.35 e⁻ in
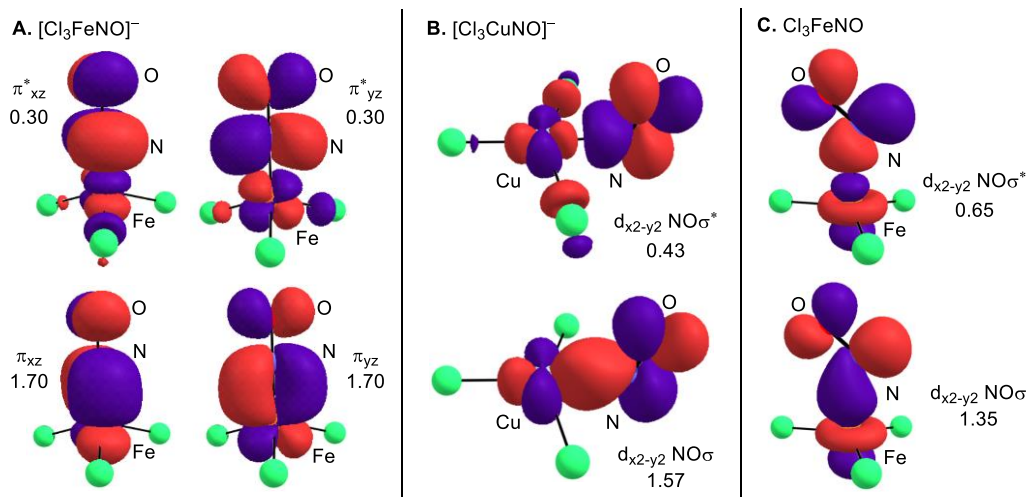
Figure 5. Partially occupied, covalent metal−NO frontier orbitals resulting from CASSCF calculations of the electronic ground states of (A) [Cl₃FeNO]⁻ [9e,13o], (B) [Cl₃CuNO]⁻ [10e,13o], and (C) Cl₃FeNO [6e, 13o].

5

the bonding orbital and 0.65 e$^-$ in the antibonding orbital (Figure 1D), similar to [Cl$_3$CuNO]$^-$.[46] Post-localization recalculation of the CI coefficients show Cl$_3$FeNO exhibits about 93% Fe^{III}-NO$^\bullet$ character as the leading configuration, and Fe^{II}-NO$^+$ contributes about 4.6% to the ground state as the second leading configuration. The increase in NO$^+$ character in the Cl$_3$FeNO complex as compared to the [Cl$_3$FeNO]$^-$ anion is consistent with our experimental observation that the Fe^{III} complex, but not Fe^{II}, is able to mediate an oxidative coupling reaction to form S-nitrosothiols.

SUMMARY AND CONCLUSIONS

In contrast to the RS$^\bullet$ expulsion mechanism from the κ^1-N RSNO species invoked during NO$^\bullet$ release from SNP, reaction of the high-spin [Cl$_3$Fe^{II}]$^-$ motif with S-nitrosothiol generates iron(III) thiolate and free NO$^\bullet$. Detailed in situ spectroscopic studies, including UV-vis, Mossbauer, and IR, suggest that coordination of the S-atom to the iron(II) center is necessary to promote S-N bond cleavage. Importantly, iron(III) chloride complexes can also promote the formation of S-nitrosothiol when NO$^\bullet$ is in excess. Our CASSCF results, when paired alongside our experimental studies, highlight the possibility of the use of computation to predict the NO$^{-/\bullet/+}$ reactivity of a series of metal nitrosyl complexes.

One central question that remains unanswered within the literature is how Fe centers promote the storage of NO$^\bullet$ as S-nitrosothiols, while also being efficient for the decomposition of RSNOs to NO$^\bullet$ and disulfide. We believe the answer to this question lies within the ability of NO$^\bullet$ to irreversibly bind to the Fe^{II} center ligated by weak field ligands,[34–37] shutting down coordination of S-nitrosothiol, which is a crucial step in its decomposition (Scheme 3). Since [Cl$_3$FeNO]$^-$ can be easily converted to the DNIC [Cl$_2$Fe(NO)$_2$]$^-$ in the presence of excess NO$^\bullet$,[39] our study also provides a potential explanation for the formation of DNIC and S-nitrosothiol frequently observed during cellular protein S-nitrosation,[10,11] and demonstrate a strategy available to nature to reversibly modulate biological NO$^\bullet$ concentration with labile iron ions.

ASSOCIATED CONTENT

The Supporting information is available free of charge on the ACS Publications website at DOI:.

Experimental details, including characterization data, spectra, computational procedures and results.

Crystallographic data for TBA$_3$[Cl$_6$Fe$^{II}_2$]•[Cl$_3$Fe^{II}(H$_2$O)] (CSD: 2057290)

AUTHOR INFORMATION

Corresponding Author

*zhang.8941@osu.edu

Notes

The authors declare no competing financial interest.

ACKNOWLEDGMENT

REFERENCES

(1) Ignarro, L. J. *Nitric Oxide: Biology and Pathobiology*; Elsevier: Amsterdam, 2009.

(2) Rassaf, T.; Kleinbongard, P.; Preik, M.; Dejam, A.; Gharini, P.; Lauer, T.; Erckenbrecht, J.; Duschin, A.; Schulz, R.; Heusch, G.; Feelisch, M.; Kelm, M. Plasma Nitrosothiols Contribute to the Systemic Vasodilator Effects of Intravenously Applied NO: Experimental and Clinical Study on the Fate of NO in Human Blood. *Circ. Res.* **2002**, *91*, 470–477.

(3) Broniowska, K. A.; Hogg, N. The Chemical Biology of S-Nitrosothiols. *Antioxidants Redox Signal.* **2012**, *17*, 969–980.

(4) Hess, D. T.; Matsumoto, A.; Kim, S. O.; Marshall, H. E.; Stamler, J. S. Protein S-Nitrosylation: Purview and Parameters. *Nat. Rev. Mol. Cell. Biol.* Nature Publishing Group February 2005, pp 150–166.

(5) Anand, P.; Stamler, J. S. Enzymatic Mechanisms Regulating Protein S-Nitrosylation: Implications in Health and Disease. *J. Mol. Med.* **2012**, *90*, 233–244.

(6) Melzer, M. M.; Mossin, S.; Cardenas, A. J. P.; Williams, K. D.; Zhang, S.; Meyer, K.; Warren, T. H. A Copper(II) Thiolate from Reductive Cleavage of an S-Nitrosothiol. *Inorg. Chem.* **2012**, *51*, 8658–8660.

(7) Zhang, S.; Çelebi-Ölçüm, N.; Melzer, M. M.; Houk, K. N.; Warren, T. H. Copper(I) Nitrosyls from Reaction of Copper(II) Thiolates with S-Nitrosothiols: Mechanism of NO Release from RSNOs at Cu. *J. Am. Chem. Soc.* **2013**, *135*, 16746–16749.

(8) Zhang, S.; Melzer, M. M.; Sen, S. N.; Çelebi-Ölçüm, N.; Warren, T. H. A Motif for Reversible Nitric Oxide Interactions in Metalloenzymes. *Nat. Chem.* **2016**, *8*, 663–669.

(9) Zhang, C.; Biggs, T. D.; Devarie-Baez, N. O.; Shuang, S.; Dong, C.; Xian, M. S-Nitrosothiols: Chemistry and Reactions. *Chem. Commun.* **2017**, *53*, 11266–11277.

(10) Li, Q.; Li, C.; Mahtani, H. K.; Du, J.; Patel, A. R.; Lancaster, J. R. Nitrosothiol Formation and Protection against Fenton Chemistry by Nitric Oxide-Induced Dinitrosyliron Complex Formation from Anoxia-Initiated Cellular Chelatable Iron Increase. *J. Biol. Chem.* **2014**, *289*, 19917–19927.

(11) Bosworth, C. A.; Toledo, J. C.; Zmijewski, J. W.; Li, Q.; Lancaster, J. R. Dinitrosyliron Complexes and the Mechanism(s) of Cellular Protein Nitrosothiol Formation from Nitric Oxide. *Proc. Natl. Acad. Sci. U. S. A.* **2009**, *106*, 4671–4676.

(12) Hottinger, D. G.; Beebe, D. S.; Kozhimannil, T.; Prielipp, R. C.; Belani, K. G. Sodium Nitroprusside in 2014: A Clinical Concepts Review. *J. Anaesthesiol. Clin. Pharmacol.* **2014**, *30*, 462–471.

(13) Rhine, M. A.; Sanders, B. C.; Patra, A. K.; Harrop, T. C. Overview and New Insights into the Thiol Reactivity of Coordinated NO in {MNO}$^{6/7/8}$ (M = Fe, Co) Complexes. *Inorg. Chem.* **2015**, *54*, 9351–9366.

(14) Hunt, A. P.; Lehnert, N. The Thiolate Trans Effect in Heme {FeNO}^{6} Complexes and Beyond: Insight into the Nature of the Push Effect. *Inorg. Chem.* **2019**, *58*, 11317–11332.

(15) Goodrich, Lauren, E. Model Complexes of Cytochrome P450 NOR, 2012.

(16) Weichsel, A.; Maes, E. M.; Andersen, J. F.; Valenzuela, J. G.; Shokhireva, T. K.; Walker, F. A.; Montfort, W. R. Heme-Assisted S-Nitrosation of a Proximal Thiolate in a Nitric Oxide Transport Protein. *Proc. Natl. Acad. Sci. U. S. A.* **2005**, *102*, 594–599.

(17) Basu, S.; Keszler, A.; Azarova, N. A.; Nwanze, N.; Perlegas, A.; Shiva, S.; Broniowska, K. A.; Hogg, N.; Kim-Shapiro, D. B. A Novel Role for Cytochrome c: Efficient Catalysis of S-Nitrosothiol Formation. *Free Radic. Biol. Med.* **2010**, *48*, 255–263.

(18) Franke, A.; Stochel, G.; Suzuki, N.; Higuchi, T.; Okuzono, K.; Van Eldik, R. Mechanistic Studies on the Binding of Nitric Oxide to a Synthetic Heme-Thiolate Complex Relevant to Cytochrome P450. *J. Am. Chem. Soc.* **2005**, *127*, 5360–5375.

(19) Gao, Y.; Mossing, B.; Wu, G. Direct NMR Detection of the Unstable "Red Product" from the Reaction between Nitroprusside and 2-Mercaptosuccinic Acid. *Dalt. Trans.* **2015**, *44*, 20338–20343.

(20) Schwane, J. D.; Ashby, M. T. FTIR Investigation of the Intermediates Formed in the Reaction of Nitroprusside and Thiolates. *J. Am. Chem. Soc.* **2002**, *124*, 6822–6823.

(21) Perissinotti, L. L.; Estrin, D. A.; Leitus, G.; Doctorovich, F. A Surprisingly Stable S-Nitrosothiol Complex. *J. Am. Chem. Soc.* **2006**, *128*, 2512–2513.

(22) Hosseininasab, V.; McQuilken, A. C.; Bakhoda, A. (Gus); Bertke, J. A.; Timerghazin, Q. K.; Warren, T. H. Lewis Acid Coordination Redirects S-Nitrosothiol Signaling Output. *Angew. Chemie* **2020**, *132*, 10946–10950.

(23) Timerghazin, Q. K.; Peslherbe, G. H.; English, A. M. Resonance Description of S-Nitrosothiols: Insights into Reactivity. *Org. Lett.* **2007**, *9*, 3049–3052.

(24) Hendinejad, N.; Timerghazin, Q. K. Biological Control of: S -Nitrosothiol Reactivity: Potential Role of Sigma-Hole Interactions. *Phys. Chem. Chem. Phys.* **2020**, *22*, 6595–6605.

(25) Roncaroli, F.; Van Eldik, R.; Olabe, J. A. Release of NO from Reduced Nitroprusside Ion. Iron-Dinitrosyl Formation and NO-Disproportionation Reactions. *Inorg. Chem.* **2005**, *44*, 2781–2790.

(26) Petrat, F.; de Groot, H.; Sustmann, R.; Rauen, U. The Chelatable Iron Pool in Living Cells: A Methodically Defined Quantity. *Biol. Chem.* **2002**, *383*, 489–502.

(27) Lok, H. C.; Sahni, S.; Jansson, P. J.; Kovacevic, Z.; Hawkins, C. L.; Richardson, D. R. A Nitric Oxide Storage and Transport System That Protects Activated Macrophages from Endogenous Nitric Oxide Cytotoxicity. *J. Biol. Chem.* **2016**, *291*, 27042–27061.

(28) Damasceno, F. C.; Condeles, A. L.; Lopes, A. K. B.; Facci, R. R.; Linares, E.; Truzzi, D. R.; Augusto, O.; Toledo, J. C. The Labile Iron Pool Attenuates Peroxynitrite-Dependent Damage and Can No Longer Be Considered Solely a pro-Oxidative Cellular Iron Source. *J. Biol. Chem.* **2018**, *293*, 8530–8542.

(29) Kruszewski, M. Labile Iron Pool: The Main Determinant of Cellular Response to Oxidative Stress. *Mutat. Res. - Fundam. Mol. Mech. Mutagen.* **2003**, *531*, 81–92.

(30) Fitzpatrick, J.; Kim, E. Synthetic Modeling Chemistry of Iron-Sulfur Clusters in Nitric Oxide Signaling. *Acc. Chem. Res.* **2015**, *48*, 2453–2461.

(31) Tran, C. T.; Kim, E. Acid-Dependent Degradation of a [2Fe-2S] Cluster by Nitric Oxide. *Inorg. Chem.* **2012**, *51*, 10086–10088.

(32) Crack, J. C.; Smith, L. J.; Stapleton, M. R.; Peck, J.; Watmough, N. J.; Buttner, M. J.; Buxton, R. S.; Green, J.; Oganesyan, V. S.; Thomson, A. J.; Le Brun, N. E. Mechanistic Insight into the Nitrosylation of the [4Fe-4S] Cluster of WhiB-like Proteins. *J. Am. Chem. Soc.* **2011**, *133*, 1112–1121.

(33) Harrop, T. C.; Tonzetich, Z. J.; Reisner, E.; Lippard, S. J. Reactions of Synthetic [2Fe-2S] and [4Fe-4S] Clusters with Nitric Oxide and Nitrosothiols. *J. Am. Chem. Soc.* **2008**, *130*, 15602–15610.

(34) McQuilken, A. C.; Matsumura, H.; Dürr, M.; Confer, A. M.; Sheckelton, J. P.; Siegler, M. A.; McQueen, T. M.; Ivanović-Burmazović, I.; Moënne-Loccoz, P.; Goldberg, D. P. Photoinitiated Reactivity of a Thiolate-Ligated, Spin-Crossover Nonheme {FeNO}^{7} Complex with Dioxygen. *J. Am. Chem. Soc.* **2016**, *138*, 3107–3117.

(35) Ting-Wah Chu, C.; Yip-Kwai Lo, F.; Dahl, L. F. Synthesis and Stereochemical Analysis of the [Fe$_4$(NO)$_4$(μ$_3$-S)$_4$]n Series (n = 0,−1) Which Possesses a Cubanelike Fe$_4$S$_4$ Core: Direct Evidence for the Antibonding Tetrametal Character of the Un. *J. Am. Chem. Soc.* **1982**, *104*, 3409–3422.

(36) Harrop, T. C.; Song, D.; Lippard, S. J. Interaction of Nitric Oxide with Tetrathiolato Iron(II) Complexes: Relevance to the Reaction Pathways of Iron Nitrosyls in Sulfur-Rich Biological Coordination Environments. *J. Am. Chem. Soc.* **2006**, *128*, 3528–3529.

(37) Conradie, J.; Quarless, D. A.; Hsu, H. F.; Harrop, T. C.; Lippard, S. J.; Koch, S. A.; Ghosh, A. Electronic Structure and FeNO Conformation of Nonheme Iron-Thiolate-NO Complexes: An Experimental and DFT Study. *J. Am. Chem. Soc.* **2007**, *129*, 10446–10456.

(38) Sun, J. S.; Zhao, H.; Ouyang, X.; Clérac, R.; Smith, J. A.; Clemente-Juan, J. M.; Gómez-Garcia, C.; Coronado, E.; Dunbar, K. R. Structures, Magnetic Properties, and

Reactivity Studies of Salts Containing the Dinuclear Anion $[M_2Cl_6]^{2-}$ (M = Mn, Fe, Co). *Inorg. Chem.* **1999**, *38*, 5841–5855.

(39) In-Iam, A.; Wolf, M.; Wilfer, C.; Schaniel, D.; Woike, T.; Klüfers, P. {FeNO}[7]-Type Halogenido Nitrosyl Ferrates: Syntheses, Bonding, and Photoinduced Linkage Isomerism. *Chem. Eur. J.* **2019**, *25*, 1304–1325.

(40) Kohlschütter, V.; Sazanoff, P. Zur Kenntnis Der Metallnitrosoverbindungen. *Berichte der Dtsch. Chem. Gesellschaft* **1911**, *44*, 1423–1432.

(41) Begel, S.; Puchta, R.; Sutter, J.; Heinemann, F. W.; Dahlenburg, L.; Eldik, R. Van. Studies on the Reaction of Iron(II) with NO in a Noncoordinating Ionic Liquid. *Inorg. Chem.* **2015**, *54*, 6763–6775.

(42) Steimann, M.; Nagel, U.; Grenz, R.; Beck, W. Die Struktur von Trichloronitrosylferrat,[Fe(NO)Cl₃]⁻. *J. Organomet. Chem.* **1983**, *247*, 171–174.

(43) Ivanova, L. V.; Cibich, D.; Deye, G.; Talipov, M. R.; Timerghazin, Q. K. Modeling of S-Nitrosothiol–Thiol Reactions of Biological Significance: HNO Production by S-Thiolation Requires a Proton Shuttle and Stabilization of Polar Intermediates. *ChemBioChem* **2017**, *18*, 726–738.

(44) Khomyakov, D. G.; Timerghazin, Q. K. Toward Reliable Modeling of S-Nitrosothiol Chemistry: Structure and Properties of Methyl Thionitrite (CH₃SNO), an S-Nitrosocysteine Model. *J. Chem. Phys.* **2017**, *147*, 44305.

(45) Melzer, M. M.; Jarchow-Choy, S.; Kogut, E.; Warren, T. H. Reductive Cleavage of O-, S-, and N-Organonitroso Compounds by Nickel(I) β-Diketiminates. *Inorg. Chem.* **2008**, *47*, 10187–10189.

(46) Bower, J. K.; Sokolov, A. Y.; Zhang, S. Four-Coordinate Copper Halonitrosyl {CuNO}[10] Complexes. *Angew. Chem. Int. Ed.* **2019**, *58*, 10225–10229.

(47) Wright, A. M.; Wu, G.; Hayton, T. W. Structural Characterization of a Copper Nitrosyl Complex with a {CuNO}[10] Configuration. *J. Am. Chem. Soc.* **2010**, *132*, 14336–14337.

(48) Tomson, N. C.; Crimmin, M. R.; Petrenko, T.; Rosebrugh, L. E.; Sproules, S.; Christopher Boyd, W.; Bergman, R. G.; Debeer, S.; Dean Toste, F.; Wieghardt, K. A Step beyond the Feltham-Enemark Notation: Spectroscopic and Correlated Ab Initio Computational Support for an Antiferromagnetically Coupled M(II)-(NO)⁻ Description of Tp*M(NO) (M = Co, Ni). *J. Am. Chem. Soc.* **2011**, *133*, 18785–18801.

(49) Monsch, G.; Klüfers, P. $[Fe(H_2O)_5(NO)]^{2+}$, the "Brown-Ring" Chromophore. *Angew. Chem. Int. Ed.* **2019**, *58*, 8566–8571.

(50) Griffith, W. P.; Lewis, J.; Wilkinson, G. Some Nitric Oxide Complexes of Iron and Copper. *J. Chem. Soc.* **1958**, 3993–3998.

(51) Radón, M.; Broclawik, E.; Pierloot, K. Electronic Structure of Selected {FeNO}[7] Complexes in Heme and Non-Heme Architectures: A Density Functional and Multireference Ab Initio Study. *J. Phys. Chem. B* **2010**, *114*, 1518–1528.

(52) Lehnert, N.; Fujisawa, K.; Camarena, S.; Dong, H. T.; White, C. J. Activation of Non-Heme Iron-Nitrosyl Complexes: Turning up the Heat. *ACS Catal.* American Chemical Society November 1, 2019, pp 10499–10518.
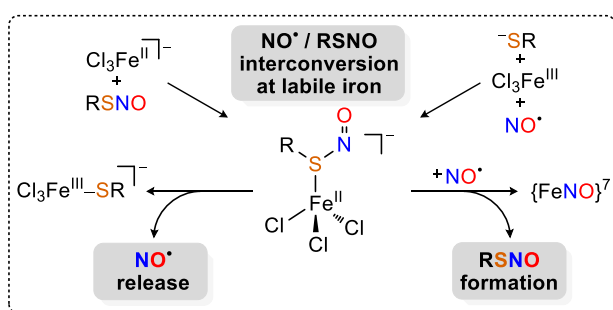
Synopsis: Simple Fe^{II}/Fe^{III} chloride salt can mediate the reversible interconversion of NO• and *S*-nitrosothiols via Fe-S interaction. This new mechanism is different from the one previously proposed for NO• release from the "red product" κ^1-N bound *S*-nitrosothiol Fe^{II} complex, $[(CN)_5Fe(\kappa^1\text{-N-RSNO})]^{3-}$.

Electronic Supporting Information for:

Iron (II/III) Halide Complexes Promote the Interconversion of Nitric Oxide and *S*-nitrosothiols through Reversible Fe-S Interaction

Anna L. Poptic,[a] and Shiyu Zhang[a]

[a]Department of Chemistry and Biochemistry, The Ohio State University, 100 W 18th Avenue, Columbus, Ohio 43210, USA

Contents:

General Experimental Details

All syntheses and experiments were performed under a nitrogen atmosphere in an MBraun glovebox or using standard Schlenk techniques unless otherwise noted. Acetonitrile, tetrahydrofuran and diethyl ether were dried and degassed under nitrogen using a Pure Process Technologies (PPT, Nashua, NH) solvent purification system, and stored over 4 Å molecular sieves. Extra dry methanol and acetone were purchased from Fischer Scientific or Sigma Aldrich and used as received. All glassware was dried at 120 °C prior to use. Elemental analysis was performed by Midwest Micro Lab (Indianapolis, IN, http://midwestlab.com/). Tetrabutylammonium chloride salt (TBACl,), bis(triphenylphosphorylene)iminium chloride (PPNCl), anhydrous iron(II) chloride, iron(III) chloride, trimethylsilyl triflate (TMSOTf), *tert*-butyl mercaptan, and triphenylmethyl mercaptan were obtained from Fischer, Alfa Aesar, or Sigma-Aldrich, and used without further purification. ^{57}Fe(0) (95%+) and Na^{15}NO$_2$ (^{15}N 98%+) were obtained from Cambridge Isotope Laboratories and used without further purification. Nitric oxide gas was purchased from Praxair and purified with Ascarite (8-20 mesh, Sigma-Aldrich) before use. NaS^{t}Bu and NaSCPh$_3$ were obtained from the corresponding thiol and NaO^{t}Bu in THF.[1] TBA(SCPh$_3$) was synthesized via cation exchange with the corresponding sodium thiolate and TBACl in THF. Ph$_3$CSNO[2], Ph$_3$CS^{15}NO[3], TBA[Cl$_4$Fe^{III}][4], ^{57}Fe^{II}Cl$_2$[5], and ^{57}Fe^{III}Cl$_3$[6] were prepared based on literature procedures. Labeled ^{15}NO was generated from ferrocene, Na^{15}NO$_2$ and trimethylsilyl trifluoromethanesulfonate (TMSOTf) based on a previously reported literature procedure.[7]

General Spectroscopic Details

^{1}H NMR spectra were recorded on a Bruker Avance NEO 400 MHz instrument or Bruker Avance III HD 600 MHz instrument and referenced to the NMR residual solvent peaks. NMR yields were calculated using trimethoxybenzene as the internal standard. UV-vis spectra were collected on an Agilent Cary 60 spectrophotometer outfitted with a Unisoku Unispeks cryostat (−100 °C to + 100 °C). In-situ solution-phase infrared spectroscopy studies were conducted with a Mettler Toledo RiRI15 spectrometer. ^{57}Fe Mössbauer spectra were measured on a constant acceleration spectrometer (SEE Co. Minneapolis, MN) with a Janis SHI-4 cryostat. Isomer shifts are quoted relative to α-Fe foil (<25 μm thick) at room temperature. Data were analyzed using the WMOSS version F software package.[8]

**Synthesis and Characterization of PPN$_2$[Cl$_6$Fe$^{II}_2$]**

PPN$_2$[Cl$_6$Fe$_2$] was prepared according to a modified literature procedure.[9] PPNCl (0.9212 g, 1.605 mmol) was dissolved in methanol (ca. 2 mL) and added to a stirring suspension of Fe^{II}Cl$_2$ (0.2034 g, 1.605 mmol, 1 equiv.) in acetone (ca. 10 mL). Upon addition of PPNCl, the mixture became a yellow homogenous solution, then a yellow suspension after stirring for 1 hour. The solution was filtered through a plug of Celite, and the Celite pad was washed with additional acetone (3 × 2 mL) to ensure complete transfer. After concentration of the filtrate under vacuum, diethyl ether (ca. 3 mL) was layered on top and the vial was placed in a −35 °C freezer. The colorless crystals that formed overnight were collected by filtration and dried under vacuum to yield PPN$_2$[Cl$_6$Fe$_2$] (1.0232 g, 91.0%). The identity of the compound was confirmed by unit cell analysis of the single crystals by X-ray diffractometry.[9]

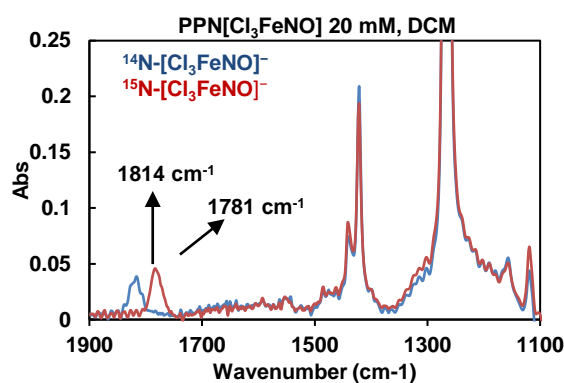**Synthesis and Characterization of PPN[Cl$_3$FeNO] ({FeNO}^{7})**

PPN[Cl$_3$FeNO] was prepared according to a modified literature procedure.[10] Solid PPN$_2$[Cl$_6$Fe$^{II}_2$] (31.0 mg, 28.4 µmol) was dissolved in a minimum amount of methanol (ca. 1.5 mL). The solution was chilled in a −35 °C freezer. Gaseous NO$^•$ (20.0 mL) was bubbled through the solution until no further color change from clear to green could be observed. Diethyl ether (ca. 1.5 mL) was layered on top of this solution with a syringe. The solution was stored at −35 °C overnight to obtain dark green needle-shaped crystals (14.5 mg, 44%.). The identity of the product was confirmed via unit cell analysis of the crystals by X-ray diffractometry.[10] The PPN[Cl$_3$Fe^{15}NO] was prepared analogously with PPN$_2$[Cl$_6$Fe$^{II}_2$] and ^{15}NO. The UV-vis sample was prepared via NO injection to an CH$_3$CN solution of PPN[Cl$_3$FeNO] (2.5 mM, 3 mL, 7.5 µmol) (Figure S1). Solution IR samples were prepared by redissolving PPN[Cl$_3$FeNO] or PPN[Cl$_3$Fe^{15}NO] in DCM (20 mM, 1 mL, 20 µmol) under ambient air (Figure S2). The Mössbauer sample was prepared using approximately 30 mg of sample suspended in paratone-N oil and loaded under liquid N$_2$ to avoid air and moisture (Figure S3). Mössbauer data were collected at 4 K in the absence of an applied magnetic field.
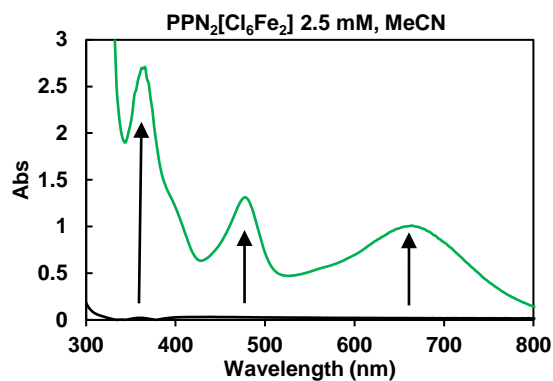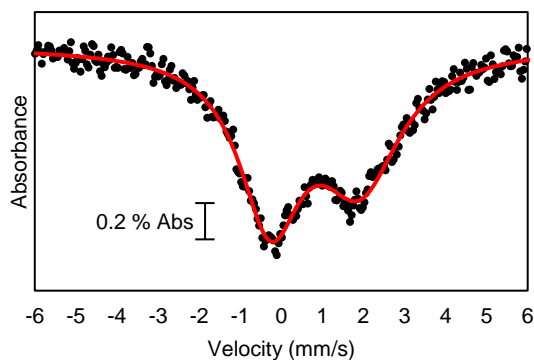
Figure S1. Reaction of $PPN_2[Cl_6Fe^{II}_2]$ with 1 eq. NO (g) to produce $PPN[Cl_3FeNO]$ (365 nm ($\varepsilon = 1080$ M^{-1} cm^{-1}), 480 nm ($\varepsilon = 500$ M^{-1} cm^{-1}), 660 nm ($\varepsilon = 400$ M^{-1} cm^{-1}).

Figure S2. Solution IR spectrum of ^{14}N and ^{15}N-$PPN[Cl_3FeNO]$.

Figure S3. ^{57}Fe Mössbauer spectrum (natural abundance) of $PPN[Cl_3FeNO]$ (4 K, 0 T). Experimenal data (black dots), best fit (red line) ($\chi^2 = 0.521$). $\delta = 0.58$ mm s-1, $|\Delta E_Q| = 1.53$ mm s^{-1}, $\Gamma_L = 1.30$, $\Gamma_R = 1.70$.

Synthesis and Characterization of $TBA_2[Cl_6Fe^{II}_2]$

$TBA_2[Cl_6Fe^{II}_2]$ was prepared in a similar manner to $PPN_2[Cl_6Fe^{II}_2]$. Under ambient air, an acetone solution of TBACl (0.5473 g, 1.969 mmol) was added to a stirred 10 mL suspension of an acetone solution of $Fe^{II}Cl_2$ (0.2496 g, 1.969 mmol). Upon addition of TBACl, the mixture

became homogenous and golden yellow. The solution was stirred overnight to give a pale yellow precipitate and a yellow solution. The solution was filtered through Celite and the precipitate was washed with acetone (3 x 2 mL). After concentration of the filtrate under vacuum, diethyl ether (ca. 3 mL) was added and the vial placed in a −35 °C freezer. The colorless crystals that formed overnight were collected by filtration and dried under vacuum to yield $TBA_2[Cl_6Fe^{II}_2]$ (0.4201 g, 53.0 %, based on Fe). The identity of the compound was determined by single-crystal x-ray diffraction. Elemental analysis, Calcd for $C_{32}H_{72}Cl_6Fe_2N_2$ C, 47.49; H, 8.97; N, 3.46. Found C, 46.84; H, 8.56; N, 3.51.

Reaction of $TBA_2[Cl_6Fe^{II}_2]$ with NO (g) in 1:1 THF/CH$_3$CN.

A solution of $TBA_2[Cl_6Fe^{II}_2]$ (3.0 mL, 0.25 mM, 0.75 µmol, 1:1 CH$_3$CN/THF) was placed in a quartz cuvette with a Schlenk attachment under a nitrogen atmosphere. NO$^\bullet$ (0.1 mL, 4.1 µmol, 5.5 equiv.) was then added to the cuvette at room temperature under a positive flow of nitrogen to generate TBA[Cl$_3$FeNO], as identified by UV-vis features at 365 nm, 480 nm, 655 nm. The molar absorbtivity values of these features are similar to those corresponding to PPN[Cl$_3$FeNO] (Figure S4).
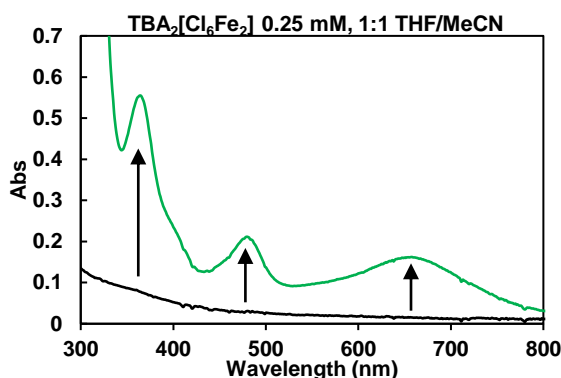
Figure S4. Reaction of $TBA_2[Cl_6Fe^{II}_2]$ with 5.5 eq. NO (g) to produce TBA[Cl$_3$FeNO] (365 nm ($\varepsilon = 1080$ M^{-1} cm^{-1}), 480 nm ($\varepsilon = 410$ M^{-1} cm^{-1}), 660 nm ($\varepsilon = 320$ M^{-1} cm^{-1}).

Solution magnetic susceptibility measurement for PPN[Cl$_3$FeNO] with Evans method

Under an inert atmosphere, a 50:1 mixture of CDCl$_3$ and CHCl$_3$ (0.800 mL) was used to prepared a 0.0275 M solution of PPN[Cl$_3$FeNO]. Separately, a few drops of the CDCl$_3$/CHCl$_3$ mixture was added to a capillary tube with one end sealed, and the capillary tube was inserted into the NMR tube of the pre-made PPN[Cl$_3$FeNO] sample. A ^{1}H NMR spectrum was acquired

(Figure S5). The magnetic susceptibility and magnetic moment were calculated and compared to theoretical values according to the equations below.

$$\chi_M = \frac{3\,\Delta f}{4\pi\,F\,c}$$

where χ_M is the molar magnetic susceptibility, Δf is the peak separation (in Hz) between two CHCl$_3$ resonances from (a) the CDCl$_3$/CHCl$_3$ pure solvent mixture in the capillary tube and (b) the CDCl$_3$/CHCl$_3$ solution of paramagnetic species, F is the spectrometer radiofrequency in Hz, and c is the concentration of the sample in mM.

$$\mu = \sqrt{8\,X_M\,T}$$

where μ is the molar magnetic susceptibility, T is the temperature (K), the constant $\sqrt{8}$ is result of $\sqrt{8} = \frac{3k_B}{N\beta^2}$ (k_B is Boltzmann's constant, N is Avogadro's number, β is the Bohr magneton of the electron (0.93×10^{-24} erg gauss^{-1}).

$$\mu_s = g\sqrt{s(s+1)}$$

where μ_s is the theoretical magnetic moment, S is the spin quantum number, g is a constant. The theoretical magnetic moment ($\mu_s = 3.873$) for systems with two unpaired electrons is in good agreement with the calculated magnetic moment for [Cl$_3$FeNO]$^-$ ($\mu = 3.936$) (Figure S5).
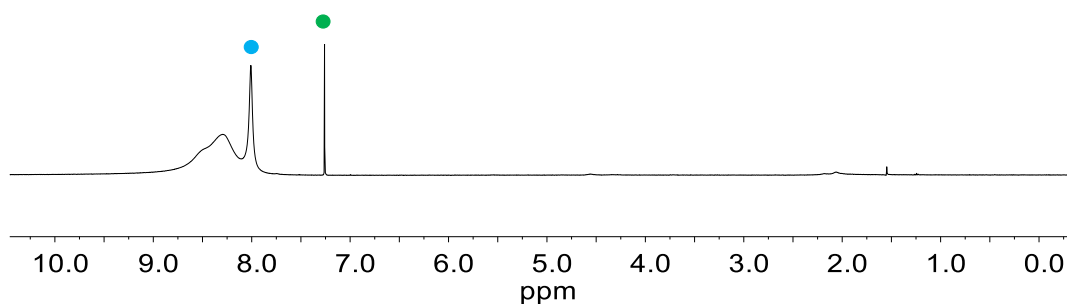
Figure S5. ^{1}H NMR (CDCl$_3$, 400 MHz) spectrum of PPN[Cl$_3$FeNO] . Green dot indicates NMR solvent (δ 7.26 – CDCl$_3$) in capillary; blue dot indicates solvent peak shift due to paramagnetic interaction with PPN[Cl$_3$FeNO] (δ 8.01) ($\Delta\delta = 0.75$ ppm).

Reaction of PPN[Cl₃FeNO] with NaSᵗBu in THF

In the glovebox, a suspension of NaSᵗBu (0.45 mL, 6.0 mM, 2.7 μmol, 3 equivalents) in THF was transferred to a quartz cuvette equipped with a rubber septum. Additional THF (2 mL) was added to the cuvette to bring the total volume to 2.7 mL. The cuvette was sealed and transferred to the UV-vis spectrometer. Under a nitrogen atmosphere, a solution of PPN[Cl₃FeNO] (0.3 mL, 3.0 mM, 0.9 μmol) was injected into the cuvette to bring the final concentrations of PPN[Cl₃FeNO] and NaSᵗBu to 0.3 mM and 0.9 mM (3 equiv.), respectively. The color of the solution quickly changed from green to deep red with λ_{max} at 360 nm and 475 nm. The red species was assigned as [(ᵗBuS)₃FeNO]⁻ based on its characteristic UV-vis features.[11] This in-situ UV-vis experiment was repeated three more times with different amounts of NaSᵗBu (1 eq., 2 eq., and 4 eq.). The overlay of the spectra is shown in Figure S6, left. A plot of absorbance at 475 nm vs. equivalents of NaSᵗBu (Figure S6, right) reveals that the stoichiometry of NaSᵗBu : PPN[Cl₃FeNO] is 3:1, further supporting that the product of the reaction is [(ᵗBuS)₃FeNO]⁻ reported by Lippard et al.[11] Based on the reported molar extinction coefficient of [(ᵗBuS)₃FeNO]⁻ at 475 nm (ε = 4360 M⁻¹cm⁻¹), the spectroscopic yield of [(ᵗBuS)₃FeNO]⁻ is 99%.
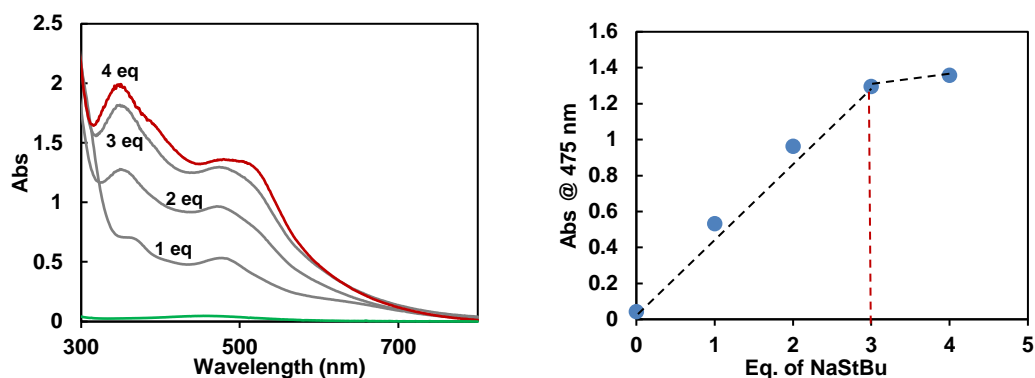
Figure S6. Left: UV-vis spectra of the reaction of PPN[Cl₃FeNO] (green trace) with different equivalents of NaSᵗBu. Right: plot of Abs (@ 475 nm) vs. equivalents of NaSᵗBu added.

Reaction of TBA₂[Cl₆Feᴵᴵ₂] with Ph₃CSNO in 1:1 CH₃CN/THF

A solution of TBA₂[Cl₆Fe₂] (2.500 mL, 0.300 mM, 0.750 μmol) was prepared in 1:1 CH₃CN/THF and transferred into a quartz cuvette with a Schlenk attachment under a nitrogen atmosphere. The cuvette was sealed and cooled to −50 ℃ in the UV-vis spectrometer. A separate

solution of Ph₃CSNO (0.500 mL, 1.500 μmol, 2 equiv.) was made under nitrogen atmosphere and injected into the cuvette to bring the final concentration of TBA$_2$[Cl$_6$Fe$_2$] and Ph$_3$CSNO to 0.250 mM and 0.500 mM (2 equiv.), respectively. The reaction was monitored by measuring one spectrum every 60 seconds at −50 °C for 30 minutes (Figure S7, left). The reaction was then warmed to room temperature and monitored for an additional 15 hours (Figure S7, right). The calculated yield of TBA[Cl$_3$FeNO] (green trace) after decomposition was close to 100%.
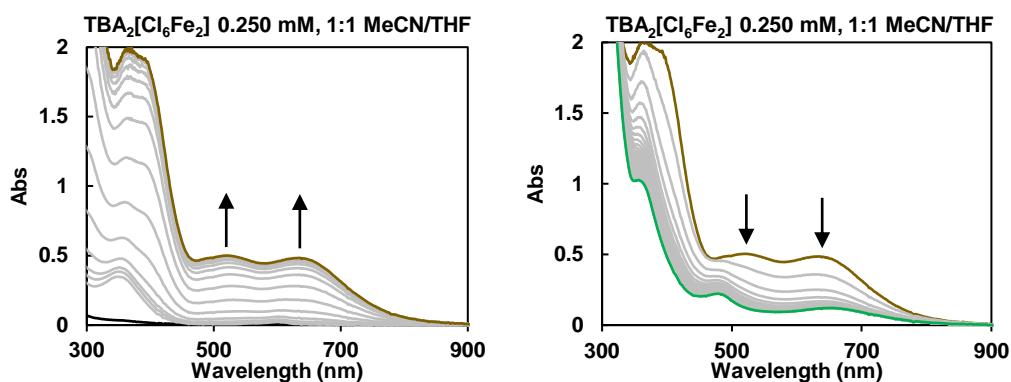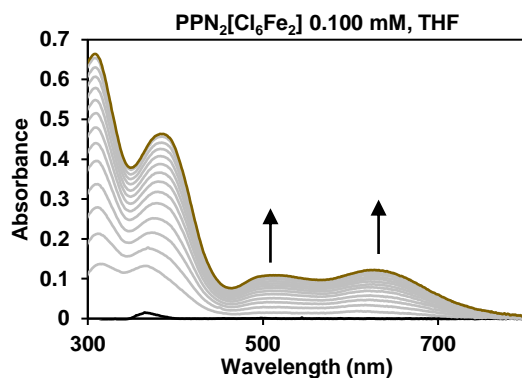

Figure S7. Left: UV-vis spectra of the reaction between TBA$_2$[Cl$_6$Fe$_2$] and Ph$_3$CSNO to form the brown intermediate. (520 nm (ε = 999 M^{-1} cm^{-1}), 630 nm (ε = 966 M^{-1} cm^{-1}).
   Right: UV-vis spetra of the decomposition of brown intermediate formed in the reaction between TBA$_2$[Cl$_6$Fe$_2$] and Ph$_3$CSNO (brown trace) over a 15-hour time period to form

Reaction of PPN$_2$[Cl$_6$Fe$^{II}_2$] with Ph$_3$CSNO in THF.

A solution of PPN$_2$[Cl$_6$Fe$_2$] (2.250 mL, 0.111 mM, 0.250 μmol) was made in THF and transferred into a quartz cuvette with a Schlenk attachment under a nitrogen atmosphere. The cuvette was sealed and cooled to −50 ºC in the UV-vis spectrometer. A separate solution of Ph$_3$CSNO (0.250 mL, 0.500 μmol, 2 equiv.) was made under nitrogen atmosphere and injected into the cuvette to bring the final concentration of PPN$_2$[Cl$_6$Fe$_2$] and Ph$_3$CSNO to 0.100 mM and 0.200 mM (2 equiv.), respectively. The reaction was monitored by measuring one UV-vis spectrum every 60 seconds for 30 minutes (Figure S8).

Figure S8. UV-vis spectra of the reaction between $PPN_2[Cl_6Fe_2]$ and Ph_3CSNO.

Reaction of TBA[Cl_4Fe^{III}] with NaSCPh$_3$ in 1:1 CH$_3$CN/THF

A solution of TBA[Cl_4Fe^{III}] (2.000 mL, 0.750 mM, 1.5 µmol) was made in a solution of 1:1 CH$_3$CN/THF and transferred into a quartz cuvette with a Schlenk attachment under a nitrogen atmosphere. The cuvette was sealed and cooled to −20 °C in the UV-vis spectrometer. A separate solution of NaSCPh$_3$ (1.000 mL, 1.5 µmol, 1 equiv.) was made under nitrogen atmosphere and injected into the cuvette under positive nitrogen flow. The UV-vis spectrum was measured 60 seconds after injection of NaSCPh$_3$. (Figure S9)
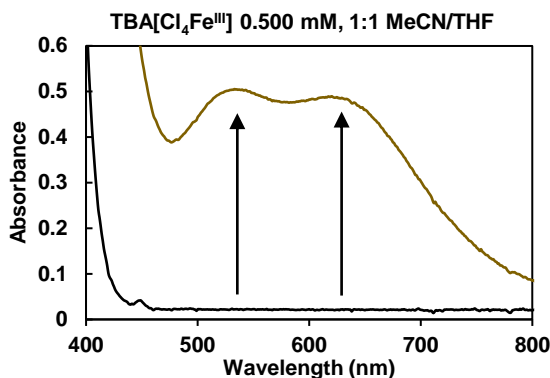
Figure S9. UV-vis spectra of the reaction between TBA[Cl_4Fe^{III}] (black) and NaSCPh$_3$ to form $[Cl_3Fe(SCPh_3)]^-$ (brown). (530 nm ($\varepsilon = 958$ M^{-1} cm^{-1}), 625 nm ($\varepsilon = 924$ M^{-1} cm^{-1}).

Reaction of Cl$_3$Fe^{III} with TBA(SCPh$_3$) in 1:1 CH$_3$CN/THF

A solution of Cl$_3$Fe^{III} (2.500 mL, 0.600 mM, 1.5 µmol) was made in a solution of 1:1 CH$_3$CN/THF and transferred into a quartz cuvette with a Schlenk attachment under a nitrogen atmosphere. The cuvette was sealed and cooled to −20 °C in the UV-vis spectrometer. A separate solution of TBA(SCPh$_3$) (0.500 mL, 1.5 µmol, 1 equiv.) was made under nitrogen atmosphere

and slowly injected into the cuvette under positive nitrogen flow (0.100 mL per min to avoid formation of any $[Cl_xFe(SCPh_3)_x]^-$). The reaction was monitored by measuring one UV-vis spectrum every 60 seconds for 30 minutes. (Figure S10).
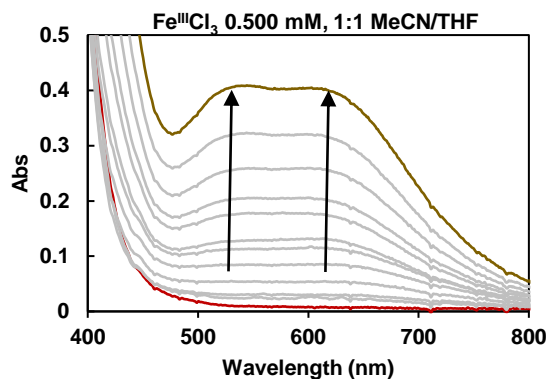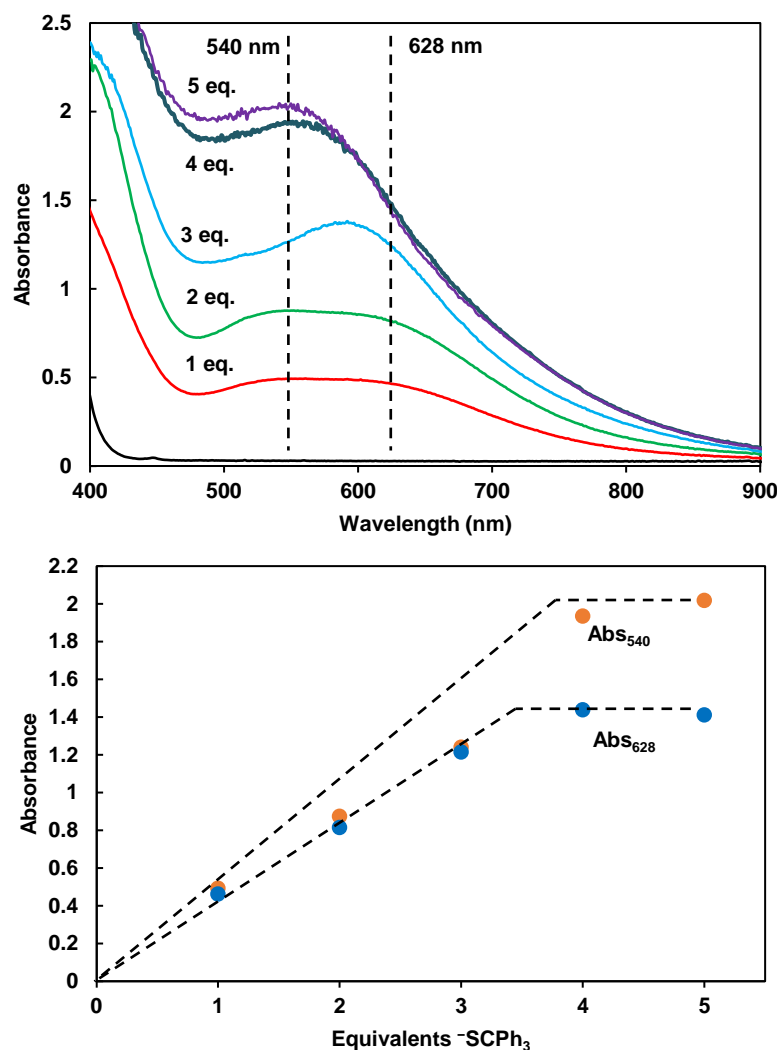

Figure S10. UV-vis spectra of the reaction between $Fe^{III}Cl_3$ (red) and TBA(SCPh$_3$) to form $[Cl_3Fe(SCPh_3)]^-$ (brown).

Determining the stoichiometry of NaSCPh$_3$ to TBA[Cl$_4$Fe^{III}] with UV-vis titration.

In glovebox, an acetonitrile solution of TBA[Cl$_4$Fe^{III}] (2.500 mL, 0.600 mM, 1.5 µmol) was transferred to a quartz cuvette equipped with a septum. The cuvette was sealed and cooled to −35 °C in the UV-vis spectrometer. The reaction mixture was titrated with sequential additions of acetonitrile solution of TBA(SCPh$_3$) (0.100 mL, 0.75 µmol, 1 eq each aliquot). The progress of the reaction was monitored by measuring one UV-vis spectrum every 60 seconds until the spectrum stabilized (Figure S11). A plot of absorbance at 540 nm and 628 nm vs. equivalents of NaSCPh$_3$ (Figure S11 bottom) suggests that the Fe^{III} center can bind up to four equivalents of thiolates.[12,13] This provides evidence for the $[Cl_3Fe^{III}(SCPh_3)]^-$ species undergoing chloride thiolate ligand scrambling, as described in Scheme S1 (below). The λ_{max} of the iron-thiolate charge transfer features (450 – 650 nm) shifts with higher concentrations of TBA(SCPh$_3$) increase, suggesting the existence of multiple $[Cl_xFe^{III}(SCPh_3)_{4-x}]^-$ species in solution.

Figure S11. Top: UV-vis spectra of the reaction between TBA[Cl$_4$Fe^{III}] with different equivalents of NaSCPh$_3$ (1 - 5 equivalents) at –35 °C in acetonitrile. All spectra were normalized by considering dilution introduced by each aliquot of NaSCPh$_3$. Bottom: plot of absorbance at 540 nm and 628 nm *vs.* equivalents of NaSCPh$_3$ added.

Determining the stoichiometry of TBA(SCPh$_3$) to Cl$_3$Fe^{III} with UV-vis titration.

In a glovebox, an acetonitrile solution of Cl$_3$Fe^{III} (2.500 mL, 0.600 mM, 1.5 µmol) was transferred to a quartz cuvette equipped with a septum. The cuvette was sealed and cooled to −35 ºC in the UV-vis spectrometer. A separate solution of TBA(SCPh$_3$) (acetonitrile, 0.500 mL, 1.5 µmol, 1 eq) was made under nitrogen atmosphere and injected into the cuvette. The color of the solution changed from orange to brown with λ$_{max}$ at 540 nm and a broad shoulder at 628 nm, which was assigned to [Cl$_3$Fe^{III}(SCPh$_3$)]⁻. The reaction mixture was titrated with sequential addition of acetonitrile solution of TBA(SCPh$_3$) (0.250 mL, 0.75 µmol, 0.5 eq each aliquot).

The progress of the reaction was monitored by measuring one UV-vis spectrum every 30 seconds until the spectrum stabilized (Figure S10). A plot of absorbance at 540 nm and 628 nm vs. equivalents of TBA(SCPh$_3$) (Figure SX bottom) suggests that the Fe^{III} center can bind up to four equivalents of thiolates.
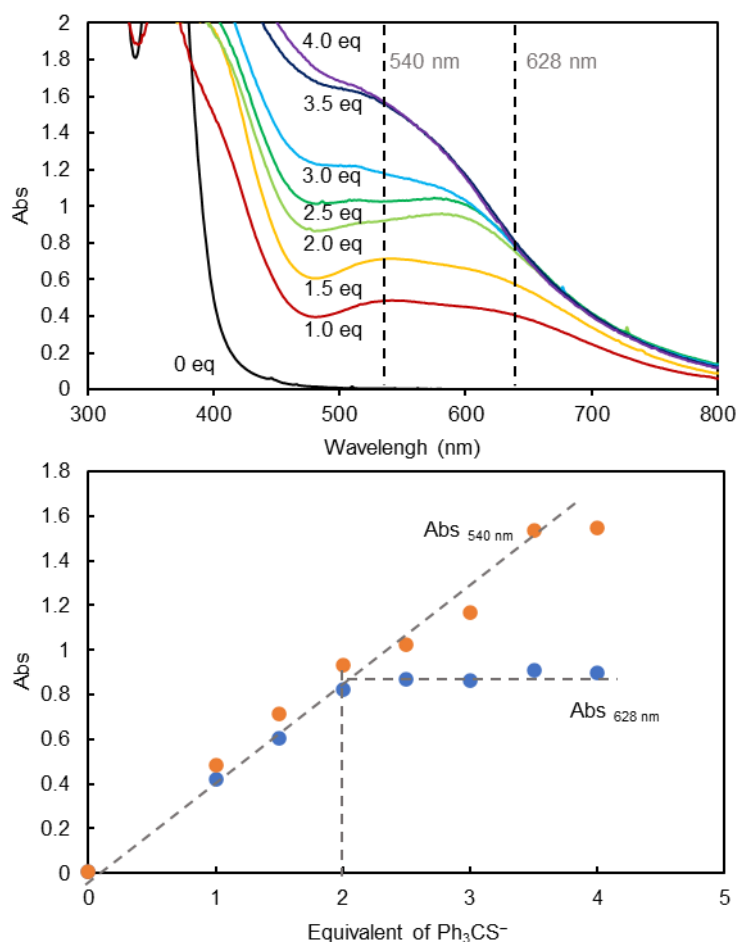
Figure S12. Top: UV-vis spectra of the reaction between Cl$_3$Fe^{III} with different equivalents of TBA(SCPh$_3$) (1 - 4 equivalents) at –35 °C in acetonitrile. All spectra were normalized by considering dilution introduced by each aliquot of TBA(SCPh$_3$). Bottom: plot of absorbance at 540 nm and 628 nm *vs.* equivalent of TBA(SCPh$_3$) added.

Scheme S1.

$$[Cl_3Fe^{III}(SCPh_3)]^- \xrightleftharpoons{K_{eq1}} \begin{array}{c} 1/2\ [Cl_2Fe^{III}(SCPh_3)_2]^- \\ + \\ 1/2\ [Cl_4Fe^{III}]^- \end{array} \xrightleftharpoons{K_{eq2}} \begin{array}{c} 1/3\ [ClFe^{III}(SCPh_3)_3]^- \\ + \\ 2/3\ [Cl_4Fe^{III}]^- \end{array} \xrightleftharpoons{K_{eq3}} \begin{array}{c} 1/4\ [Fe^{III}(SCPh_3)_3]^- \\ + \\ 3/4\ [Cl_4Fe^{III}]^- \end{array}$$
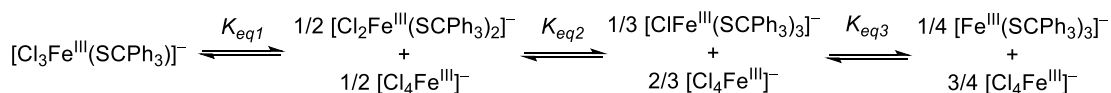
Quantification of Ph$_3$CS-SCPh$_3$ and [Cl$_6$Fe$^{II}_2$]$^{2-}$ from Fe^{III}Cl$_3$ + 1 eq. TBA(SCPh$_3$)

In the glovebox, separate solutions of Fe^{III}Cl$_3$ (9.73 mg, 0.060 mmol, 1 eq.) and TBA(SCPh$_3$) (31.1 mg, 0.060 mmol, 1 eq.) were made in MeCN. The solutions were cooled to −35 °C, then

combined and left to react at −35 °C until the brown color of the reaction had faded (48 hours). The MeCN was removed *in vacuo* and toluene was added to the solid to dissolve the disulfide that had formed. The mixture was filtered to collect the toluene filtrate, and the insoluble portion containing $TBA_2[Cl_6Fe^{II}_2]$ was recrystallized from acetone/diethyl ether. The disulfide was recrystallized from toluene/diethyl ether. The yields of disulfide and $TBA_2[Cl_6Fe^{II}_2]$ were 73.3 % (12.1 mg) and 82.7% (20.1 mg), respectively.

Synthesis and characterization of $TBA_2[Cl_6{}^{57}Fe^{II}_2]$ for Mössbauer spectroscopy

This compound was prepared according to a similar procedure to the unlabeled material. Under ambient air, an acetone solution of TBACl (27.4 mg, 98.6 μmol) was added to a stirring 2 mL suspension of an acetone solution of > 95% enriched $^{57}Fe^{II}Cl_2{}^5$ (12.6 mg, 98.6 μmol). Upon addition of TBACl, the mixture became homogenous and a golden yellow. The solution was stirred overnight to give a pale yellow precipitate and a yellow solution. The solution was filtered through Celite and the precipitate was washed with acetone (3 x 2 mL). After concentration of the filtrate *in vacuo*, diethyl ether (ca. 3 mL) was added and the vial placed in a −35 °C freezer. The colorless crystals were collected after workup correspond to $TBA_2[Cl_6{}^{57}Fe^{II}_2]$ (20.3 mg, 50.8 %, based on Fe). Successful synthesis of this material was confirmed by UV-vis monitoring of the reaction of $TBA_2[Cl_6{}^{57}Fe^{II}_2]$ with Ph_3CSNO. A solution of $TBA_2[Cl_6Fe_2]$ (2.500 mL, 0.300 mM, 0.750 μmol) was prepared in 1:1 CH_3CN/THF and transferred into a quartz cuvette with a Schlenk attachment under a nitrogen atmosphere. The cuvette was sealed and cooled to −50 ºC in the UV-vis spectrometer. A separate solution of Ph_3CSNO (0.500 mL, 1.500 μmol, 2 equiv.) was made under nitrogen atmosphere and injected into the cuvette to bring the final concentration of $TBA_2[Cl_6Fe_2]$ and Ph_3CSNO to 0.250 mM and that of 0.500 mM (2 equiv.), respectively. The reaction was monitored by measuring one UV-vis spectrum every 60 seconds at −50 °C for 30 minutes (Figure S13).

TBA$_2$[Cl$_6$Fe$_2$] 0.250 mM, 1:1 MeCN/THF
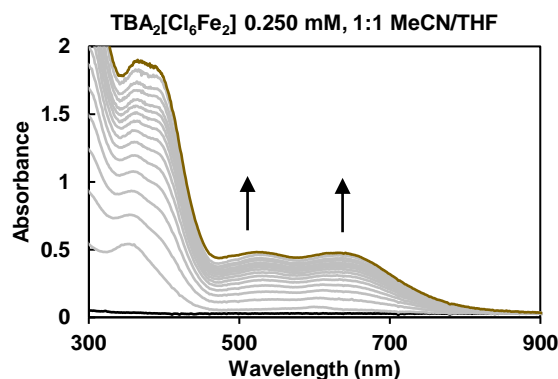
Figure S13. UV-vis spectra of the reaction between TBA$_2$[Cl$_6{}^{57}$Fe$^{II}{}_2$] (black) and Ph$_3$CSNO to form the brown intermediate. The absorption values at 520 and 630 nm were in agreement with those formed by the unlabeled material.

Solution Mössbauer of TBA$_2$[Cl$_6{}^{57}$Fe^{II}]

To a delrin Mössbauer sample cup containing 1.4 mg of TBA$_2$[Cl$_6{}^{57}$Fe^{II}] under a nitrogen atmosphere at room temperature was added 0.345 mL of 9:1 THF/MeCN to form a 5 mM solution. The sample was sealed in a vial, removed from the glovebox and frozen in liquid nitrogen. The sample was kept stored in liquid nitrogen until being loaded. The data was collected at 80 K in the absence of an applied external magnetic field (Figure S14).
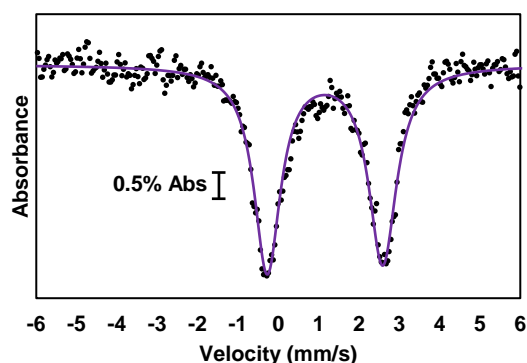
Figure S14. ^{57}Fe Mössbauer spectrum of TBA$_2$[Cl$_6{}^{57}$Fe$^{II}{}_2$] (80 K, 0 T). Experimenal data (black dots), best fit (purple) ($\chi^2 = 0.698$). $\delta = 1.16$ mm s^{-1}, $|\Delta E_Q| = 2.86$ mm s^{-1}, $\Gamma_L = 0.80$, $\Gamma_R = 0.84$.

Synthesis and characterization of TBA[Cl$_4{}^{57}$Fe^{III}] for Mössbauer spectroscopy

TBA[Cl$_4{}^{57}$Fe^{III}] was prepared according to modified literature procedures.[6,14] To 29.0 mg of ^{57}Fe powder (>95%) (0.510 mmol, 1 eq) was added 5 mL of concentrated (35%) aqueous HCl. This solution was heated to 120 °C and refluxed for 48 hrs, during which time an orange solution (Fe^{III}Cl$_3 \cdot$ 6H$_2$O) formed. Upon cooling to room temperature, one equivalent of TBACl

(0.510 mmol, 141.5 mg) was added to the solution with stirring. Immediately, a yellow precipitate formed. The yellow precipitate was collected by filtration, and rinsed with diethyl ether. The yellow precipitate was recrystallized from a mixture of dichloromethane/diethyl ether at −35 °C to yield TBA[Cl$_4$^{57}Fe^{III}] (85.2 mg, 38.0% based off Fe). The formation of TBA[Cl$_4$^{57}Fe^{III}] was verified by monitoring the reaction with NaSCPh$_3$ by UV-vis spectroscopy. A solution of TBA[Cl$_4$Fe^{III}] (2.000 mL, 0.750 mM, 1.5 μmol) was made in a solution of 1:1 CH$_3$CN/THF and transferred into a quartz cuvette with a Schlenk attachment under a nitrogen atmosphere. The cuvette was sealed and cooled to −20 °C in the UV-vis spectrometer. A separate solution of NaSCPh$_3$ (1.000 mL, 1.5 μmol, 1 equiv.) was made under nitrogen atmosphere and injected into the cuvette under positive nitrogen flow. The UV-vis spectrum was measured 60 seconds after injection of NaSCPh$_3$ (Figure S15)
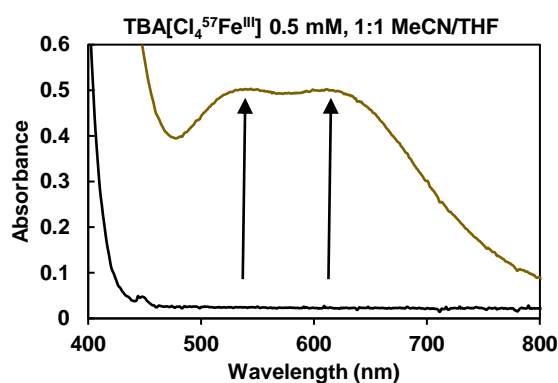
Figure S15. UV-vis spectra of the reaction between TBA[Cl$_4$^{57}Fe^{III}] (black) and NaSCPh$_3$ to form TBA[Cl$_3$^{57}Fe−SCPh$_3$]. The absorption values at 540 and 628 nm were in agreement with those formed by the unlabeled material.

Solution Mössbauer of TBA[$Cl_4$$^{57}Fe^{III}$]

To a delrin Mössbauer sample cup containing 2.1 mg of TBA[$Cl_4$$^{57}Fe^{III}$] under a nitrogen atmosphere at room temperature was added 475.6 μL of 9:1 THF/MeCN to form a 10 mM solution. The sample was sealed in a vial, removed from the glovebox and frozen in liquid nitrogen. The sample was kept stored in liquid nitrogen until being loaded. The data was collected at 80 K in the absence of an applied external magnetic field (Figure S17).
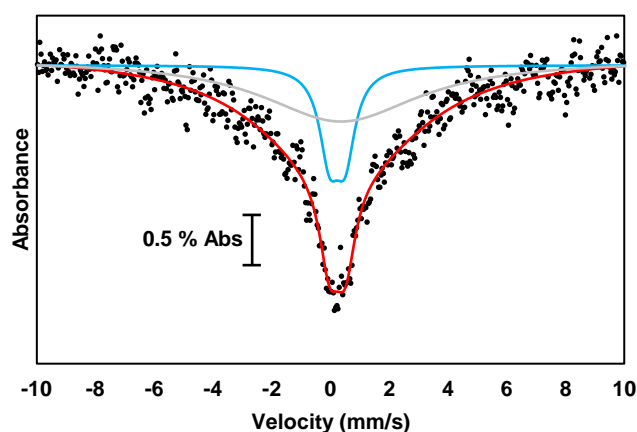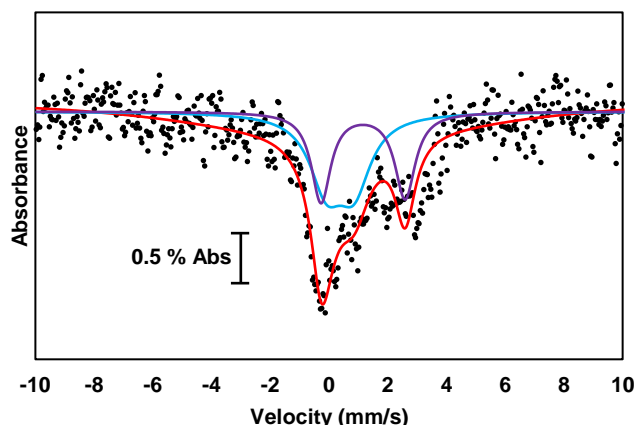

Figure S17. ^{57}Fe Mössbauer spectrum of TBA[$Cl_4$$^{57}Fe^{III}$] (80 K, 0 T). Experimenal data (black dots), best fit (red) ($\chi^2 = 0.553$). The best fit was comprised of two subsites. Subsite 1 (blue) $\delta = 0.23$ mm s^{-1}, $|\Delta E_Q| = 0.53$ mm s^{-1}, $\Gamma_L = \Gamma_R = 0.83$. Subsite 2 (grey) was added to represent the intermediate relaxation of the doublet at 80 K. $\delta = 0.36$ mm s^{-1}, $|\Delta E_Q| = 0.00$ mm s^{-1}, $\Gamma_L = \Gamma_R = 6.51$

Solution Mössbauer of the reaction of TBA$_2$[$Cl_6$$^{57}Fe^{II}_2$] + 2 Ph$_3$CSNO

Under a nitrogen atmosphere, a solution of Ph$_3$CSNO (30 mM, 0.250 mL) in 9:1 THF/CH$_3$CN was cooled to −45 °C in a delrin Mössbauer sample cup. Separately, a solution of TBA$_2$[$Cl_6$$^{57}Fe^{II}_2$] (15 mM, 0.250 mL) was cooled to −45 °C. The two solutions were mixed to make the final concentration of Fe and Ph$_3$CSNO 15 mM. Upon mixing, there was a gradual color change from green to dark brown. After allowing the reaction to proceed for 60 mins, the solvent was removed to form a thin layer of sample in the bottom of the sample cup. The sample was then frozen in liquid nitrogen and kept stored under liquid nitrogen until loading to avoid O$_2$ and moisture contamination. Mössbauer spectra were collected at 80 K in the absence of an

external magnetic field (Figure S18).

Figure S18. ^{57}Fe Mössbauer spectrum of TBA$_2$[Cl$_6$^{57}Fe$^{II}_2$] + 2 eq. Ph$_3$CSNO (80 K, 0 T). Experimenal data (black dots), best fit (red) ($\chi^2 = 0.694$) with parameters: subsite 1 (blue) matches the parameters for [Cl$_3$Fe^{III}–SCPh$_3$]$^-$ independently generated from the reaction of TBA[Cl$_4$Fe^{III}]+1 NaSCPh$_3$, $\delta = 0.38$ mm s^{-1} , $|\Delta E_Q| = 0.94$ mm s^{-1}, $\Gamma_R = \Gamma_L = 1.38$, %I = 56; subsite 2 (purple) matches the parameters of TBA$_2$[Cl$_6$^{57}Fe$^{II}_2$] $\delta = 1.16$ mm s^{-1} , $|\Delta E_Q| = 2.86$ mm s^{-1}, $\Gamma_R = 0.84$ $\Gamma_L = 0.80$, %I = 44.

Solution Mössbauer of the reaction of TBA[Cl$_4$^{57}Fe^{III}] + 1 NaSCPh$_3$

Under a nitrogen atmosphere, a solution of NaSCPh$_3$ (20 mM, 0.250 mL) in 9:1 THF/CH$_3$CN was cooled to −20 °C in a delrin Mössbauer sample cup. Separately, a solution of TBA[Cl$_4$^{57}Fe^{III}] (20 mM, 0.250 mL) was cooled to −20 °C. The two solutions were mixed to make the final concentration of Fe and NaSCPh$_3$ 10 mM. Upon mixing, there was a color change from yellow to dark brown. After allowing the reaction to occur for ten minutes, solvent was removed to form a thin layer of sample at the bottom of the sample cup. The sample cup then was frozen in liquid nitrogen and kept stored under liquid nitrogen until loading to avoid O$_2$ and moisture contamination. Mössbauer spectra were collected at 80 K in the absence of an external magnetic field (Figure S19).
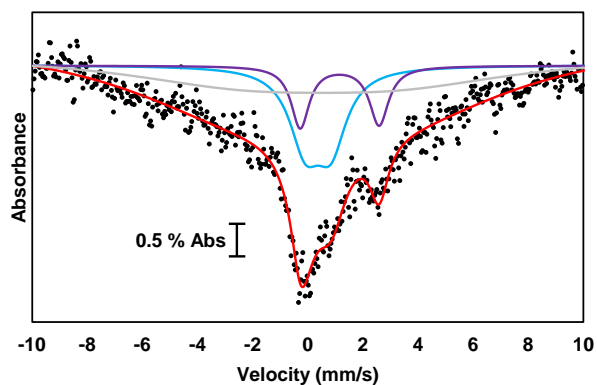
Figure S19. ^{57}Fe Mössbauer spectrum of $TBA[Cl_4{}^{57}Fe^{III}]$ + 1 eq. $NaSCPh_3$ (80 K, 0 T). Experimenal data (black dots), best fit (red) (χ^2 = 0.634) with parameters: subsite 1 (blue) δ = 0.38 mm s^{-1} , $|\Delta E_Q|$ = 0.93 mm s^{-1}, $\Gamma_R = \Gamma_L$ = 1.38, %I = 67; subsite 2 (purple) matches the parameters of $TBA_2[Cl_6{}^{57}Fe^{II}{}_2]$ δ = 1.16 mm s^{-1} , $|\Delta E_Q|$ = 2.86 mm s^{-1}, Γ_R = 0.84 Γ_L = 0.80, %I = 33. Subsite 3 (grey) was added to represent the intermediate relaxation of the doublet at 80 K. δ = 0.45 mm s^{-1}, $|\Delta E_Q|$ = 5.61 mm s^{-1}, $\Gamma_L = \Gamma_R$ = 10.78

In situ solution IR monitoring of $TBA_2[Cl_6Fe^{II}{}_2]$ + 2 eq. Ph_3CSNO in THF-d_8

A solution of Ph_3CSNO (1.000 mL, 150.0 mM, 150.0 μmol) was made in THF-d_8 under nitrogen atmosphere. The solution was injected with a syringe into a three-neck cell under flowing argon atmosphere and cooled in an acetone/dry ice bath to −78 ºC. A separate solution of $TBA_2[Cl_6Fe^{II}{}_2]$ (1.500 mL, 75 μmol, 0.5 equiv.) was made under nitrogen atmosphere and injected via syringe into the cell to make the final concentration of Ph_3CSNO and Fe 30 mM. The reaction was monitored by scanning the IR spectrum every 15 seconds for a total of 3 hrs (Figure S20)
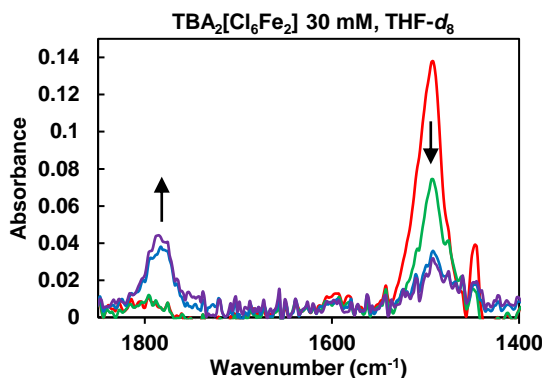
Figure S20. IR spectra (solvent background subtracted) of the reaction between TBA$_2$[Cl$_6$Fe$^{II}_2$] and 2 eq. Ph$_3$CSNO. Red trace: Ph$_3$CSNO in 1.000 mL THF-d_8 at −78 °C. Green: directly after addition of TBA$_2$[Cl$_6$Fe$^{II}_2$] in 1.500 mL THF-d_8 at −78 °C. Dark blue: After 1 hour of reaction, gradually warming solution to 0 °C. Purple: completed reaction after 3 hours. ν(NO)$_{Ph3SNO}$ = 1493 cm^{-1}; ν(NO)$_{TBA[Cl3FeNO]}$ = 1792 cm^{-1}.

In situ solution IR monitoring of TBA$_2$[Cl$_6$Fe$^{II}_2$] + 2 Ph$_3$CS^{15}NO in THF-d_8

A solution of Ph$_3$CS^{15}NO (1.500 mL, 80.0 mM, 120.0 μmol) was made in THF-d_8 under nitrogen atmosphere. The solution was injected with a syringe into a three-neck cell under flowing argon atmosphere and cooled in an acetone/dry ice bath to −78 ºC. A separate solution of TBA$_2$[Cl$_6$Fe$^{II}_2$] (0.500 mL, 60 μmol, 0.5 equiv.) was made under nitrogen atmosphere and injected via syringe into the cell to make the final concentration of Ph$_3$CS^{15}NO and Fe 30 mM. The reaction was monitored by scanning the IR spectrum every 15 seconds for a total of 3 hrs (Figure S21). ν(^{15}NO)$_{Ph3S15NO}$ = 1473 cm^{-1}; $\Delta\nu$ = 21 cm^{-1} (calculated from Hooke's law $\Delta\nu$ = 27 cm^{-1}) ν(^{15}NO)$_{TBA[Cl3Fe15NO]}$ = 1753 cm^{-1}; $\Delta\nu$ = 39 cm^{-1} (calculated from Hooke's law $\Delta\nu$ = 33 cm^{-1}).
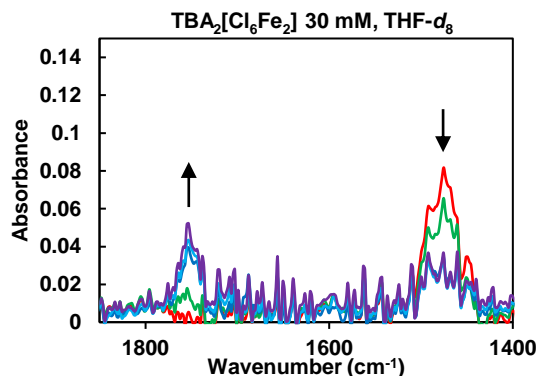
Figure S21. IR spectra (solvent background subtracted) of the reaction between TBA$_2$[Cl$_6$Fe$^{II}_2$] and 2 eq. Ph$_3$CS^{15}NO. Red trace: Ph$_3$CS^{15}NO in 1.5 mL THF-d_8 at −78 °C. Green: directly after addition of TBA$_2$[Cl$_6$Fe$^{II}_2$] in 0.5 mL THF-d_8 at −78 °C. Dark blue: After 1 hour of reaction, gradually warming solution to 0 °C. Light blue: After 1 hour 45 minutes of reaction, solution at room temperature. Purple: completed reaction after 3 hours.
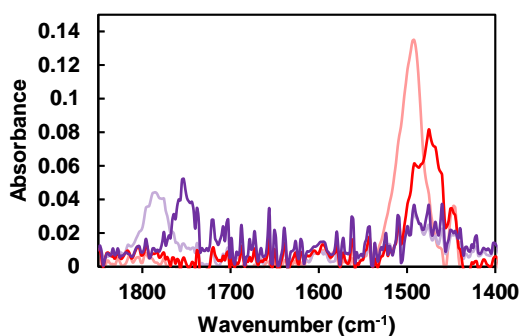
Figure S22. Overlaid IR spectra of the reaction between TBA$_2$[Cl$_6$Fe$^{II}_2$] with 2 eq. Ph$_3$CS^{15}NO (bright traces), and TBA$_2$[Cl$_6$Fe$^{II}_2$] and 2 eq. Ph$_3$CS^{14}NO (pale traces). The red and purple traces in both cases correspond to the beginning and end of the reactions, respectively.

In situ solution IR of Cl$_3$Fe^{III} + TBA(SCPh$_3$) and NO (g) in 9:1 THF-d_8/CD$_3$CN

A solution of Fe^{III}Cl$_3$ (1.250 mL, 60.0 mM, 75.0 μmol) was made in 9:1 THF-d_8/CD$_3$CN under a nitrogen atmosphere. The solution was injected with a syringe into a three-neck cell under flowing nitrogen atmosphere and cooled in an acetone/dry ice bath to −78 ºC. A separate solution of TBA(SCPh$_3$) (1.250 mL, 75.0 μmol) was made under nitrogen atmosphere and injected via syringe into the cell to make the final concentration of Fe/SCPh$_3$ 30 mM. Gaseous NO˙ 2 x 1.8 mL (1 eq. each) was added sequentially, allowing sufficient time for the spectrum to stabilize between additions. The reaction was monitored for 2 hours by scanning the IR

spectrum every 15 seconds.
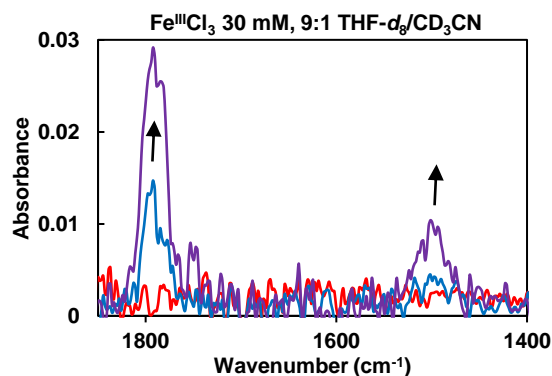
Figure S23. IR spectra (solvent background subtracted) of the reaction between $Fe^{III}Cl_3$, 1 eq. $TBA(SCPh_3)$, and 2 eq. NO (g). Red: $Fe^{III}Cl_3/TBA(SCPh_3)$ solution in 2.500 mL 9:1 THF-d_8/CD$_3$CN at −78 °C. Blue: directly after addition of the second eq. NO (g) at −78 °C. Purple: reaction solution after 2 hours, at −50 °C. The spectrum did not change after warming the solution to room temperature. $\nu(NO)_{TBA[Cl3FeNO]}$ = 1792 cm^{-1}; $\nu(NO)_{Ph3CSNO}$ = 1493 cm^{-1}.

In situ solution IR calibration curve for TBA[Cl₃FeNO] in 9:1 THF-*d₈*/CD₃CN

A solution of $TBA_2[Cl_6Fe^{II}_2]$ (0.250 mL, 15.0 mM, 3.750 μmol) was made in 9:1 THF-d_8/CD$_3$CN under a nitrogen atmosphere. The solution was injected into a three-neck cell with a syringe under flowing nitrogen atmosphere and cooled in an acetone/dry ice bath to −78 ºC . Gaseous NO$^•$ (0.18 mL, 7.500 μmol, 2 eq.) was added to form TBA[Cl₃FeNO] *in-situ* at a 30 mM concentration. Following formation of TBA[Cl₃FeNO], additional solvent was added in 0.10 mL increments (0.60 mL added total) allowing sufficient time for the spectrum to stabilize between additions (Figure SX, left). The absorbance at 1792 cm^{-1} was tracked after each addition to create a calibration curve (Figure S24 right). The yield of TBA[Cl₃FeNO] from the reaction of $Fe^{III}Cl_3$, $TBA(SCPh_3)$, and NO$^•$ was calculated to be 20.2 mM ± 0.6 mM, based on the absorbance at 1792 cm^{-1} (Figure S24)
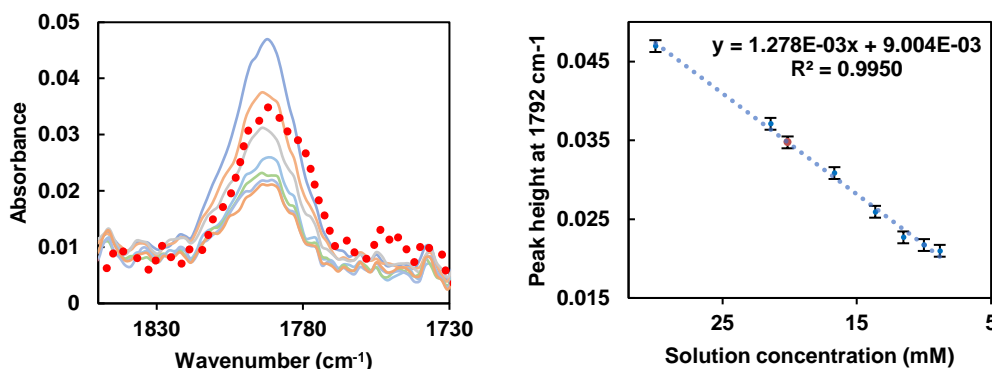
Figure S24. Left: IR spectra (solvent background subtracted) of TBA[Cl₃FeNO] at −78 °C. Each solid trace represents the dilution that occurred after each 0.10 mL addition of solvent. Red dotted trace: overlay of TBA[Cl₃FeNO] peak from the final spectrum in figure S23. Right: Calibration curve (error bars ± 1 std.dev y-direction) for TBA[Cl₃FeNO] (blue dots) with equation and R^2 value. Red dot represents the calculated yield of TBA[Cl₃FeNO].

In situ solution IR calibration curve for Ph₃CSNO in 9:1 THF-d_8/CD₃CN

A solution of Ph₃CSNO (0.250 mL, 30.0 mM, 7.500 μmol) was made in 9:1 THF-d_8/CD₃CN under a nitrogen atmosphere. The solution was injected with a syringe into a three-neck flask under flowing nitrogen atmosphere and cooled with an acetone/dry ice bath to −78 °C. Additional solvent was added in 0.10 mL increments (0.60 mL added total) allowing sufficient time for the spectrum to stabilize between additions (Figure S25, left). The absorbance was tracked at 1493 cm⁻¹ after each addition to create the calibration curve (Figure S25, right). The absorbance at 1493 cm⁻¹ from the independent reaction between Fe^{III}Cl₃ and TBA(SCPh₃) was
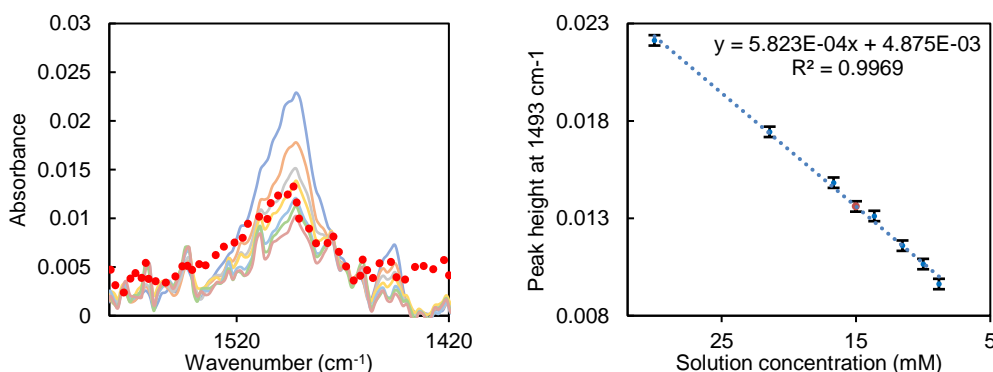
Figure S25. Left: IR spectra (solvent background subtracted) of Ph₃CSNO at −78 °C. Each solid trace represents the dilution that occurred after each 0.10 mL addition of solvent. Red dotted trace: overlay of Ph₃CSNO peak from the final spectrum in figure S23. Right: Calibration curve (error bars ± 1 std.dev y-direction) for Ph₃CSNO (blue dots) with equation and R^2 value. Red dot represents the calculated yield of Ph₃CSNO.

utilized to calculate the yield of Ph$_3$CSNO. The yield was calculated to be 15.0 mM ± 0.5 mM.

X-ray Crystallographic Data

Single crystals of each compound were mounted under paratone oil on glass fibers and immediately placed under a cold nitrogen stream (Oxford Cryosystems Cryostream) at 150(2) K on a Bruker D8 with Mo Kα radiation source (λ = 0.7107 Å) and a Photon II detector. The data was integrated with the Bruker SAINT program. Structure solutions were performed using the SHELXTL/PC suite[15] under XSEED[16] or Olex2 program, and were corrected for Lorentz and polarization effects. An empirical absorption correction was applied using Blessing's method as incorporated into the program SADABS.[17] Non-hydrogen atoms were refined with anisotropic thermal parameters and hydrogen atoms were included in idealized positions. Structures were rendered with POV-Ray in XSEED using 50% probability ellipsoids.
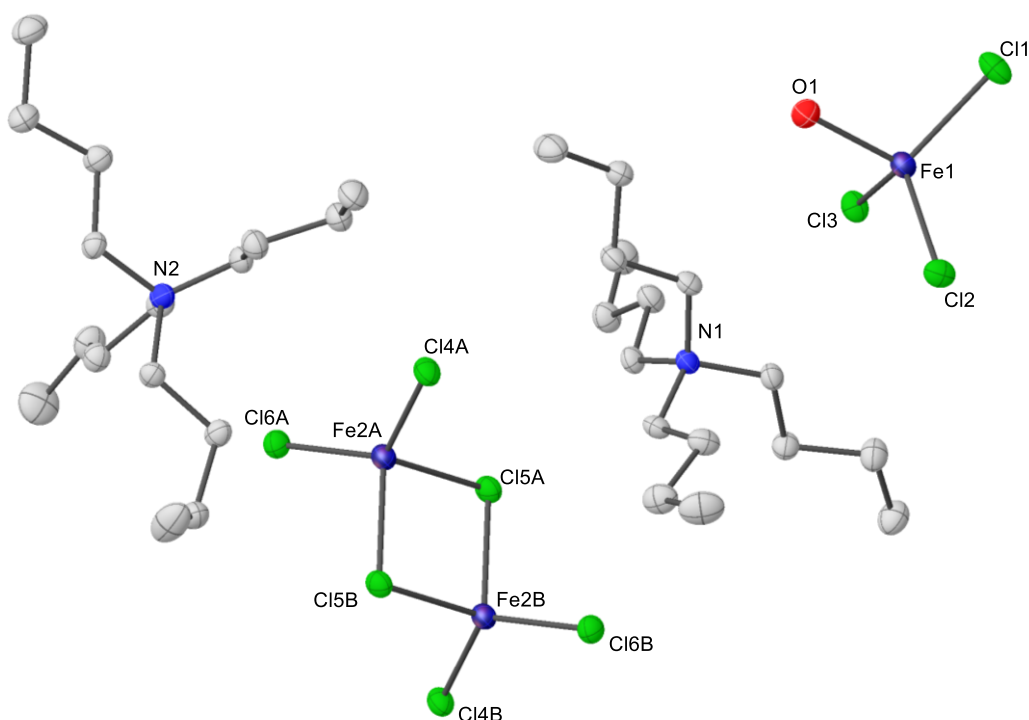
Figure S26. X-ray structure of TBA$_3$[Cl$_6$Fe$^{II}_2$]•[Cl$_3$Fe^{II}(H$_2$O)] with thermal ellipsoids of 30% probability. An Et$_2$O solvent molecule is omitted. Only ½[Cl$_6$Fe$^{II}_2$]$^{2-}$ is contained in the unit cell, however, the full dimeric structure is shown for clarity, with the two [Cl$_3$Fe^{II}]$^-$ sites denoted A and B.

Computational Methodology

All computations were performed using Gaussian16 or ORCA 4.1.0.[18] The initial geometry optimization for the ground states of $[Cl_3FeNO]^-$ and $[Cl_3CuNO]^-$ were carried out using the (U)BP86[19,20] method with the def2-TZVP basis set, starting from coordinates obtained from the single crystal structures.[21] The initial geometry optimization for Cl_3FeNO in the $S = 0, 1, 2$ spin states was performed using the (U)BP86[19,20], (U)B3LYP[19], and TPSSh[22] functionals and def2-TZVPP basis set, although further calculations were carried out with the optimized geometry obtained from the TPSSh/def2-TZVP optimization. Coordinates of optimized compounds along with their energies (in Hartree) are reported. All geometry optimizations were performed using tight convergence thresholds for the energy (10^{-6} E_h) and maximum value of the energy nuclear gradient (3×10^{-4} E_h/a_0).[23] Multireference calculations were performed using the complete active space self-consistent field (CASSCF) method.[24,25] In all CASSCF computations, the def2-TZVP basis set was used. For the initial reference CASSCF wavefunction of $[Cl_3FeNO]^-$ an active space of 9 electrons in 13 orbitals was used, for $[Cl_3CuNO]^-$, an active space of 10 electrons in 13 orbitals, and Cl_3FeNO, an active space of 6 electrons in 13 orbitals. After CASSCF computations, a valence-bond like interpretation of the wavefunction was performed on each complex to qualitatively determine the contributions of different resonance structures, i.e. $Fe(III)\text{-}NO^-$, $Fe(II)\text{-}NO^•$. To this end, a localization of the CASSCF natural orbitals was done, followed by a CAS-CI expansion of the wavefunction. Only CSF's with a coefficient larger than 0.01 were included in these analyses, which reproduced about 95% of the total CAS wavefunction in each case. The localization procedure (using the Cholesky algorithm)[26] was only performed on orbitals with a significant contribution from both NO and the metal. In most cases this was the combination of metal $3d_{xz,yz,z2}$ orbitals with NO $\pi_{x,y}^*$. The resulting localized orbitals became either majority metal-based or NO-based, and it is important to note that the usage of these orbitals in the CAS-CI expansion of the wave function did not change the overall CAS wave function, only simplified the intuitive, qualitative interpretation in terms of valence-bond, resonance-like interpretations. Configurations with sufficiently high coefficients (larger than 0.1%), were classified into one of three major resonance structures, $M^{n+1}\text{-}NO^-$, $M^n\text{-}NO^•$, or $M^{n-1}\text{-}NO^+$. Coefficients corresponding to the same resonance structure were added together to produce the amount each contributed to the overall ground state.

Calculated spectra **for [Cl₃Fe(SMe)]⁻ by TD-DFT**

I.   TPSSh/def2-TZVP Optimized structure (in XYZ format, Å)

Energy = -3082.937579517106

Fe	0.026996000	0.000075000	0.001670000
Cl	1.791985000	0.468617000	-1.304033000
Cl	-0.430506000	1.692784000	1.375345000
Cl	-1.717617000	-0.505990000	-1.311550000
S	0.491675000	-1.779620000	1.310019000
C	0.693508000	-3.144655000	0.108058000
H	-0.210690000	-3.251869000	-0.490647000
H	1.545346000	-2.948627000	-0.542927000
H	0.869291000	-4.060550000	0.672950000
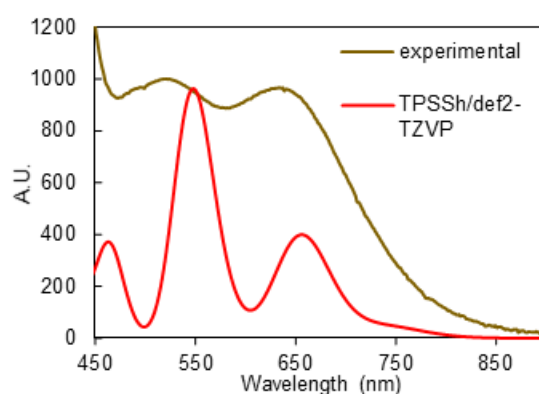
Figure S27. TD-DFT absorption spectrum of [Cl₃Fe(SMe)]⁻. TPSSh/def2-TZVP (red) with optimized geometry from the same functional/basis set. These calculated spectra are overlaid with the experimental data of the brown intermediate formed in the reaction between $[Cl_6Fe^{II}_2]^{2-}$ and Ph_3CSNO (Figure S7).

[Cl₃FeNO]⁻ (S = 3/2) electronic structure calculations

II.   BP86/def2-TZVP Optimized structure (in XYZ format, Å)

Energy = -2774.999359741336

Fe	0.000713000	0.000559000	-0.018025000
Cl	-0.683093000	2.011583000	-0.753112000
Cl	-1.393497000	-1.599966000	-0.758218000
Cl	2.089574000	-0.408781000	-0.740276000
O	0.015793000	0.000144000	2.863216000
N	-0.000039000	0.000182000	1.684604000

CASSCF(9,13)/def2-TZVP calculation results

Energy = -2770.6109816645

III.   Contour plots of the occupied active orbitals (with occupation numbers) resulting from CASSCF(9,13). External (unoccupied) active orbitals are omitted.
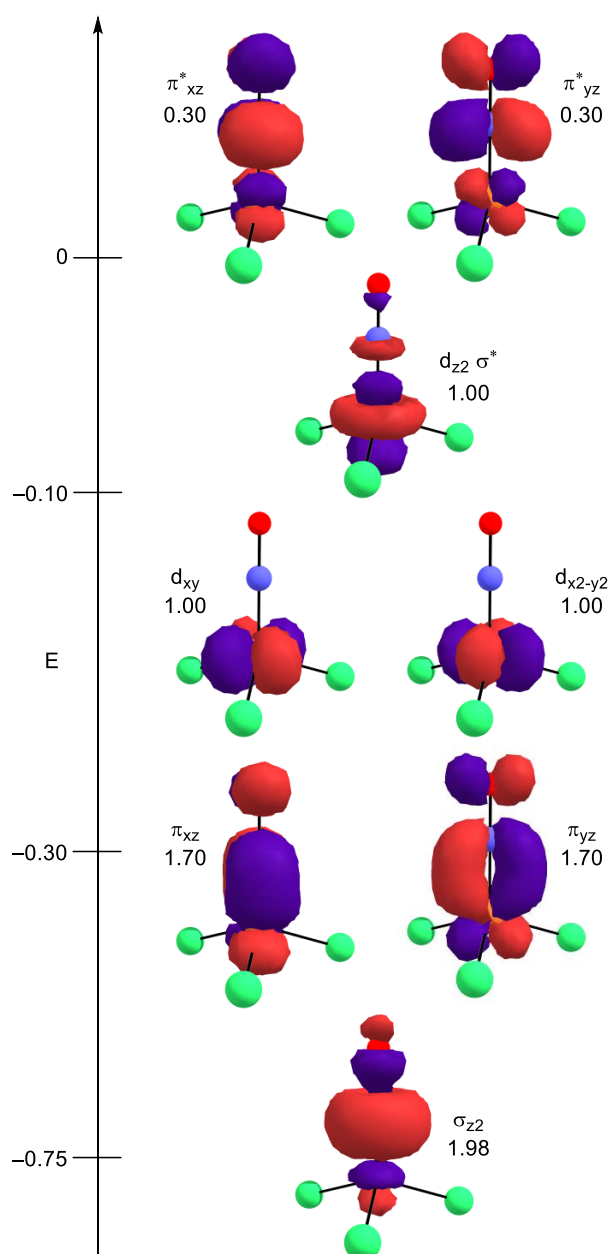
IV.   Pipek-Mezey localization of covalent Fe 3d−NOπ* orbitals
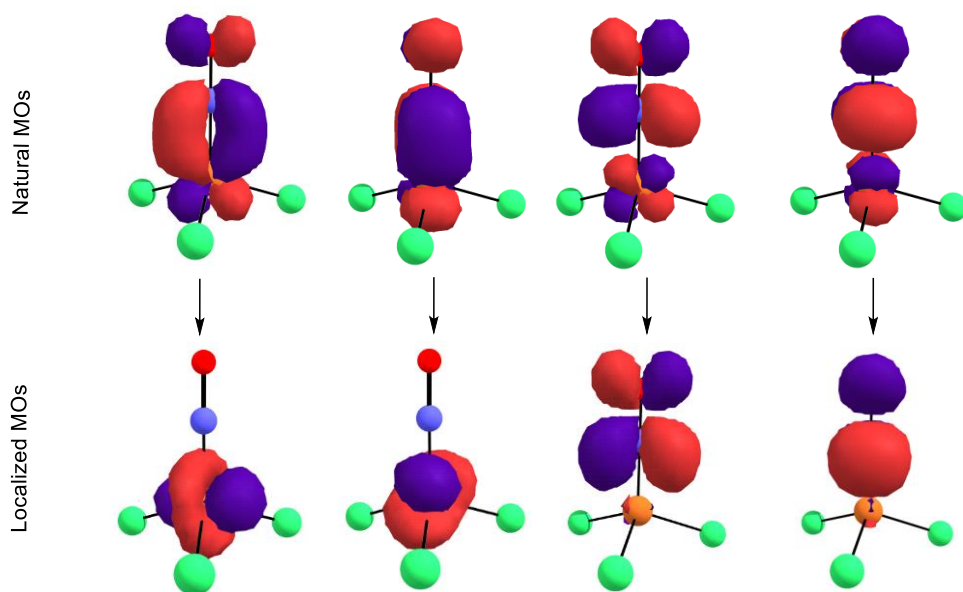
V. Leading configurations[a,b] in the basis of localized Fe 3d−NOπ* (Energy of recalculated wavefunction = -2770.6109816778 Eh)

Fe d_{xz}	Fe d_{yz}	Fe d_{x2-y2}	Fe d_{xy}	Fe d_{z2}	NO p_x	NO p_y	Character	Weight
up	up	up	up	up	down	down	Fe(III)−NO⁻	46.349%
2	up	up	up	up	0	down	Fe(II)−NO•	15.880%
up	2	up	up	up	down	0	Fe(II)−NO•	15.742%

[a]Additional CSFs with smaller coefficients corresponding to the same Fe−NO interactions were added together to arrive at the final weights of each electronic configuration.

[b]The Fe-NO σ bonding orbital is omitted from this table, as the occupation consistently remained 2.

VI. Final weights of the contribution of each resonance structure in [Cl₃FeNO]⁻

Character	Weight
Fe(IV)−NO²⁻	0.804 %
Fe(III)−NO⁻	51.942 %
Fe(II)−NO•	39.987 %
Fe(I)−NO⁺	2.003 %
others	5.264 %

[Cl₃CuNO]⁻ (S = 1/2) electronic structure calculations

I.   BP86/def2-TZVP Optimized structure (in XYZ format, Å)

Energy = −3151.776633291106

|			
Cu	-0.004659000	0.000000000	-0.005801000
Cl	0.570032000	-2.159543000	0.249660000
Cl	-2.214884000	0.000000000	-0.315269000
Cl	0.570032000	2.159543000	0.249660000
N	2.012279000	0.000000000	0.099010000
O	2.602220000	0.000000000	-0.903483000

CASSCF(10,13)/def2-TZVP Calculation results

Energy = -3147.1628378855

II.   Contour plots of the occupied active orbitals (with occupation numbers) resulting from CASSCF(10,13). External (unoccupied) active orbitals are omitted.
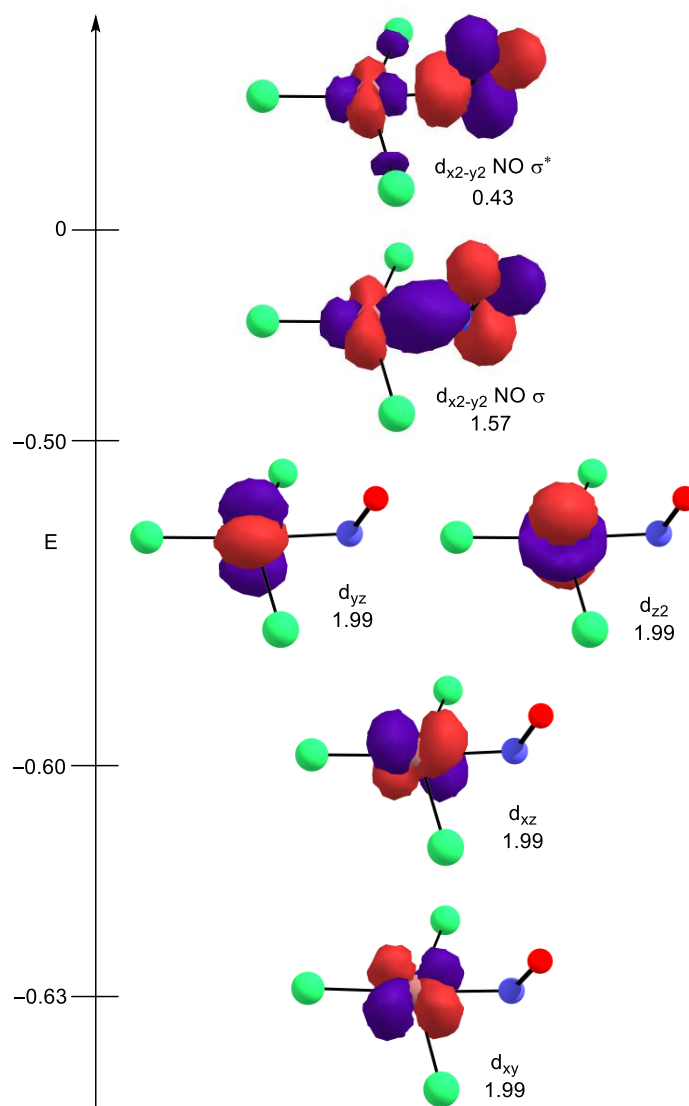
III.   Pipek-Mezey localization of covalent Cu−NO orbitals
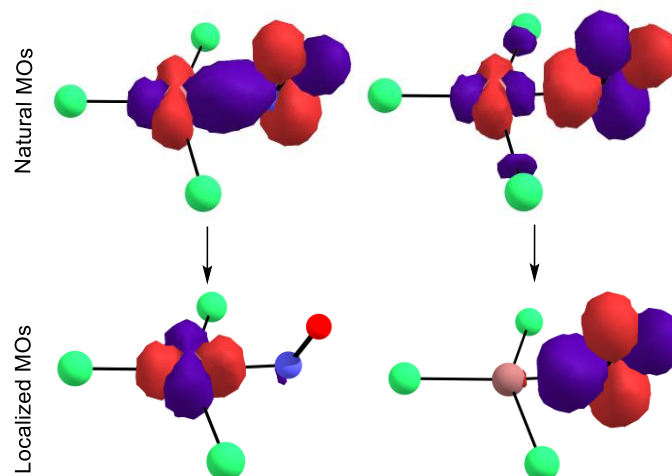
IV.   Leading CAS-CI configurations[a] in the basis of localized Cu 3d−NO

Cu d_{xz}	Cu d_{yz}	Cu d_{x2-y2}	Cu d_{xy}	Cu d_{z2}	NO π^*_x	NO π^*_y	Character	Weight
2	2	up	2	2	down	0	Cu(II)−NO$^•$	86.374%
2	2	2	2	2	0	0	Cu(I)−NO$^+$	9.650%
2	2	2	2	0	2	0	Cu(III)−NO$^-$	1.1165%

[a]There were no additional CSF's to add in the Cu-NO case

V.   Final weights of each electronic configuration for [Cl$_3$CuNO]$^-$

Character	Weight
Cu(III)−NO$^-$	1.1165%
Cu(II)−NO$^•$	86.374%
Cu(I)−NO$^+$	9.650%
others	2.8595%

Cl$_3$Fe^{III}NO (S = 2) electronic structure calculations

I.   TPSSh/def2-TZVP Optimized Structure (in XYZ format, Å)

Energy = -2774.553148464734
Fe   11.614799000   9.074563000   13.987725000
Cl   13.486452000   9.885622000   13.239533000

| Cl | 10.555486000 | 10.064671000 | 15.604176000 |
Cl	10.401116000	7.980873000	12.574742000
O	12.516805000	6.460939000	14.830414000
N	12.517340000	7.576332000	15.048410000

II.   CASSCF(6,13)/def2-TZVP calculation results

Energy = -2770.462644901734

III.   Contour plots of the occupied active orbitals (with occupation numbers) resulting from CASSCF(6,13).

IV.   Pipek-Mezey localization of covalent Fe 3d−NO σ/σ* orbitals

Natural MOs
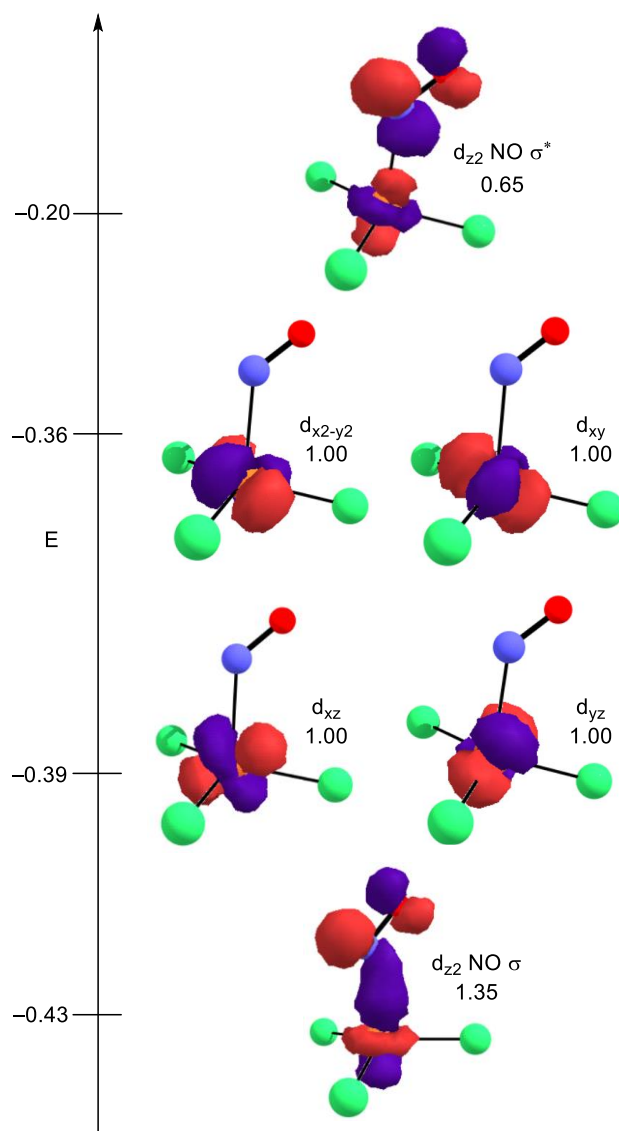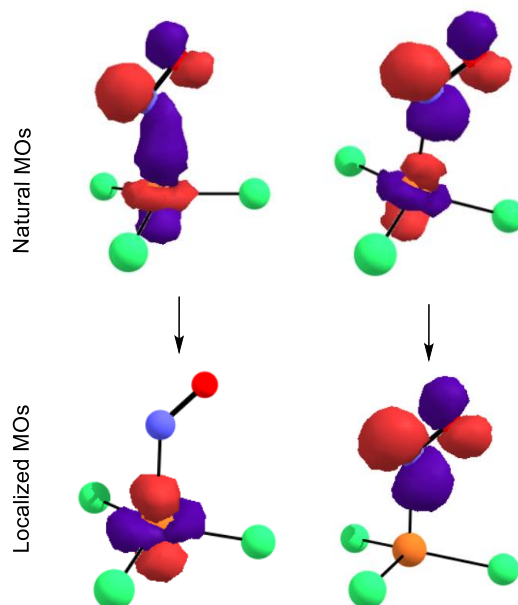
Localized MOs

V.   Leading CAS-CI configurations[a] in the basis of localized Fe 3d−NO σ/σ*

Fe d_{z2}	Fe d_{xz}	Fe d_{yz}	Fe d_{x2-y2}	Fe d_{xy}	NO π^*_x	Character	Weight
up	up	up	up	up	down	Fe(III)−NO$^{\bullet}$	93.161%
2	up	up	up	up	0	Fe(II)−NO$^+$	4.640%

[a]Additional CSFs corresponding to the same Fe−NO interactions were added together to arrive at the final weights of each electronic configuration.

VI.   Final weights of each electronic configuration for Cl$_3$Fe^{III}NO

Character	Weight
Fe(III)−NO$^{\bullet}$	93.161%
Fe(II)−NO$^+$	4.640%
Fe(IV)−NO$^-$	0.257%
Others	1.942%

References

(1) Groysman, S.; Holm, R. H. A Series of Mononuclear Quasi-Two-Coordinate Copper(l) Complexes Employing a Sterically Demanding Thiolate Ligand. *Inorg. Chem.* **2009**, *48*, 621–627.

(2) Melzer, M. M.; Mossin, S.; Cardenas, A. J. P.; Williams, K. D.; Zhang, S.; Meyer, K.; Warren, T. H. A Copper(II) Thiolate from Reductive Cleavage of an S-Nitrosothiol. *Inorg. Chem.* **2012**, *51*, 8658–8660.

(3) Arulsamy, N.; Bohle, D. S.; Butt, J. A.; Irvine, G. J.; Jordan, P. A.; Sagan, E. Interrelationships between Conformational Dynamics and the Redox Chemistry of S-Nitrosothiols. *J. Am. Chem. Soc.* **1999**, *121*, 7115–7123.

(4) Hay, M. T.; Geib, S. J. Tetrabutylammonium Tetrachloroferrate(III). *Acta Crystallogr. Sect. E Struct. Reports Online* **2005**, *61*, m190–m191.

(5) Carlson, M. R.; Gray, D. L.; Richers, C. P.; Wang, W.; Zhao, P. H.; Rauchfuss, T. B.; Pelmenschikov, V.; Pham, C. C.; Gee, L. B.; Wang, H.; Cramer, S. P. Sterically Stabilized Terminal Hydride of a Diiron Dithiolate. *Inorg. Chem.* **2018**, *57*, 1988–2001.

(6) Comba, P.; Gahan, L. R.; Mereacre, V.; Hanson, G. R.; Powell, A. K.; Schenk, G.; Zajaczkowski-Fischer, M. Spectroscopic Characterization of the Active Fe IIIfe III and Fe IIIfe II Forms of a Purple Acid Phosphatase Model System. *Inorg. Chem.* **2012**, *51*, 12195–12209.

(7) Cardenas, A. J. P.; Culotta, B. J.; Warren, T. H.; Grimme, S.; Stute, A.; Fröhlich, R.; Kehr, G.; Erker, G. Capture of NO by a Frustrated Lewis Pair: A New Type of Persistent N-Oxyl Radical. *Angew. Chemie - Int. Ed.* **2011**, *50*, 7567–7571.

(8) Vinet, L.; Zhedanov, A. A "missing" Family of Classical Orthogonal Polynomials. *Journal of Physics A: Mathematical and Theoretical*. 2011, pp 1689–1699.

(9) Sun, J. S.; Zhao, H.; Ouyang, X.; Clérac, R.; Smith, J. A.; Clemente-Juan, J. M.; Gómez-Garcia, C.; Coronado, E.; Dunbar, K. R. Structures, Magnetic Properties, and Reactivity Studies of Salts Containing the Dinuclear Anion $[M_2Cl_6]^{2-}$ (M = Mn, Fe, Co). *Inorg. Chem.* **1999**, *38*, 5841–5855.

(10) In-Iam, A.; Wolf, M.; Wilfer, C.; Schaniel, D.; Woike, T.; Klüfers, P. $\{FeNO\}^7$-Type Halogenido Nitrosyl Ferrates: Syntheses, Bonding, and Photoinduced Linkage

Isomerism. *Chem. - A Eur. J.* **2019**, *25*, 1304–1325.

(11)   Harrop, T. C.; Song, D.; Lippard, S. J. Interaction of Nitric Oxide with Tetrathiolato Iron(II) Complexes: Relevance to the Reaction Pathways of Iron Nitrosyls in Sulfur-Rich Biological Coordination Environments. *J. Am. Chem. Soc.* **2006**, *128*, 3528–3529.

(12)   Chang, S.; Koch, S. A. [Fe^{III}(SR)$_4$]$^{1-}$ Complexes Can Be Synthesized by the Direct Reaction of Thiolates with FeCl3. *J. Inorg. Biochem.* **2007**, *101*, 1758–1759.

(13)   Holm, R. H.; Lo, W. Structural Conversions of Synthetic and Protein-Bound Iron-Sulfur Clusters. *Chem. Rev.* **2016**, *116*, 13685–13713.

(14)   Hay, M. T.; Geib, S. J. Tetrabutylammonium Tetrachloroferrate(III). *Acta Crystallogr. Sect. E Struct. Reports Online* **2005**, *61*, m190–m191.

(15)   Bruker-Analytical X-ray Services. SHELXTL-PC, Vers. 5.10. Universität Göttingen: Göttingen, Germany 1998.

(16)   Barbour, L. XSEED. 1999.

(17)   Blessing, R. H. An Empirical Correction for Absorption Anisotropy. *Acta Crystallogr. Sect. A* **1995**, *51*, 33–38.

(18)   Neese, F. Software Update: The ORCA Program System, Version 4.0. *Wiley Interdiscip. Rev. Comput. Mol. Sci.* **2018**, *8*, e1327.

(19)   Becke, A. D. *Density-Functional Exchange-Energy Approximation with Correct Asymptotic Behavior*; 1988; Vol. 38.

(20)   Perdew, J. P. *Density-Functional Approximation for the Correlation Energy of the Inhomogeneous Electron Gas*; 1986; Vol. 33.

(21)   Weigend, F.; Ahlrichs, R. Balanced Basis Sets of Split Valence, Triple Zeta Valence and Quadruple Zeta Valence Quality for H to Rn: Design and Assessment of Accuracy. *Phys. Chem. Chem. Phys.* **2005**, *7*, 3297–3305.

(22)   Tao, J.; Perdew, J. P.; Staroverov, V. N.; Scuseria, G. E. Climbing the Density Functional Ladder: Nonempirical Meta–Generalized Gradient Approximation Designed for Molecules and Solids. *Phys. Rev. Lett.* **2003**, *91*.

(23)   Grimme, S.; Antony, J.; Ehrlich, S.; Krieg, H. A Consistent and Accurate Ab Initio Parametrization of Density Functional Dispersion Correction (DFT-D) for the 94 Elements H-Pu. *J. Chem. Phys.* **2010**, *132*, 154104.

(24)   Werner, H. J.; Knowles, P. J. A Second Order Multiconfiguration SCF Procedure with
         Optimum Convergence. *J. Chem. Phys.* **1985**, *82*, 5053–5063.

(25)   Knowles, P. J.; Werner, H. J. An Efficient Second-Order MC SCF Method for Long
         Configuration Expansions. *Chem. Phys. Lett.* **1985**, *115*, 259–267.

(26)   Aquilante, F.; Bondo Pedersen, T.; Sánchez De Merás, A.; Koch, H. Fast Noniterative
         Orbital Localization for Large Molecules. *J. Chem. Phys.* **2006**, *125*, 174101.

Gaussian16 full reference:

Gaussian 16, Revision C.01, Frisch, M. J.; Trucks, G. W.; Schlegel, H. B.; Scuseria, G. E.; Robb, M. A.; Cheeseman, J. R.; Scalmani, G.; Barone, V.; Petersson, G. A.; Nakatsuji, H.; Li, X.; Caricato, M.; Marenich, A. V.; Bloino, J.; Janesko, B. G.; Gomperts, R.; Mennucci, B.; Hratchian, H. P.; Ortiz, J. V.; Izmaylov, A. F.; Sonnenberg, J. L.; Williams-Young, D.; Ding, F.; Lipparini, F.; Egidi, F.; Goings, J.; Peng, B.; Petrone, A.; Henderson, T.; Ranasinghe, D.; Zakrzewski, V. G.; Gao, J.; Rega, N.; Zheng, G.; Liang, W.; Hada, M.; Ehara, M.; Toyota, K.; Fukuda, R.; Hasegawa, J.; Ishida, M.; Nakajima, T.; Honda, Y.; Kitao, O.; Nakai, H.; Vreven, T.; Throssell, K.; Montgomery, J. A., Jr.; Peralta, J. E.; Ogliaro, F.; Bearpark, M. J.; Heyd, J. J.; Brothers, E. N.; Kudin, K. N.; Staroverov, V. N.; Keith, T. A.; Kobayashi, R.; Normand, J.; Raghavachari, K.; Rendell, A. P.; Burant, J. C.; Iyengar, S. S.; Tomasi, J.; Cossi, M.; Millam, J. M.; Klene, M.; Adamo, C.; Cammi, R.; Ochterski, J. W.; Martin, R. L.; Morokuma, K.; Farkas, O.; Foresman, J. B.; Fox, D. J. Gaussian, Inc., Wallingford CT, 2016.